Comparative Analysis of Nonlinear Viscoelastic Models Across Common Biomechanical Experiments

Will Zhang[1] · Adela Capilnasiu[2] · David Nordsletten[1,2] (ID)

Abstract

Biomechanical modeling has a wide range of applications in the medical field, including in diagnosis, treatment planning and tissue engineering. The key to these predictive models are appropriate constitutive equations that can capture the stress-strain response of materials. While most applications rely on hyperelastic formulations, experimental evidence of viscoelastic responses in tissues and new numerical techniques has spurred the development of new viscoelastic models. Classical as well as fractional viscoelastic formulations have been proposed, but it is often difficult from the practitioner perspective to identify appropriate model forms. In this study, a systematic examination of classical and fractional nonlinear isotropic viscoelastic models is presented (consider six primary forms). Consideration is given for common testing paradigms, including varying strain or stress loading and dynamic conditions. Models are evaluated across model parameter spaces to assess the range of behaviors exhibited in these different forms across all tests. Similarity metrics are introduced to compare thousands of models, with exemplars for each type of model presented to illustrate the response and behavior of different model variants. The parameter analysis does not only identify how the models can be tailored, but also informs on the model complexity and fidelity. These results illustrate where these common models yield physical and non-physical behavior across a wide range of tests, and provide key insights for deciding on the appropriate viscoelastic modeling formulations.

✉ D. Nordsletten
nordslet@umich.edu

W. Zhang
willwz@umich.edu

A. Capilnasiu
adela.capilnasiu@kcl.ac.uk

[1]   Department of Biomedical Engineering, University of Michigan, Ann Arbor, USA

[2]   School of Biomedical Engineering and Imaging Sciences, King's College London, London, UK
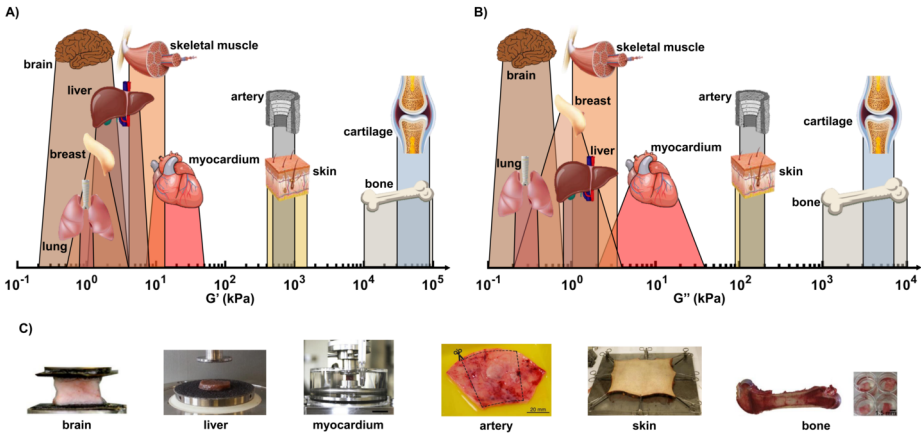
Fig. 1 Illustration of the storage and loss modulus for common biomaterials. **A**) Storage modulus for common biomaterials adapted from Budday et al. [21]. **B**) Loss modulus for brain [13, 22, 39], lung [118], breast [133], liver [88, 122], skeletal muscle [141], myocardium [106, 121], skin [62, 79], artery [81, 129], cartilage [42] and bone [18]. **C**) Examples of tissues in rheological testing - brain [21] in shear testing device, liver [9] in torsion device, myocardium in triaxial shear device [136], artery [24], skin in multiaxial device [52] and bone [70]

1 Introduction

Accurate biomechanical model of tissues has a wide range of applications in medicine, such as patient-specific modeling, treatment planning, tissue engineering and in vivo tissue assessment. In particular, patient-specific models have been employed to understand a range of conditions, including mechanical properties and functions of the heart [6, 7, 25, 59, 83, 112], mechanical function of cardiac valves [2, 126], response to diseased abdominal aortic aneurysms and dissection [50, 119, 132], and collision mechanics in the brain [53, 156]. Appropriate tissue models enable pre-operative planning through simulations and have been deployed for bone implants [29, 55, 107], artery stent insertion [5, 40, 54], and surgical training [93], amongst other applications. They are also critical for diagnostic methods such as magnectic resonance elastography (MRE) [82, 94, 133, 134, 148], which rely on models to translate wave motion into local tissue properties. In addition, characterization of tissues using such models also plays an important role in tissue engineering and fabrication of biocompatible materials [77, 158]. A common thread through all applications is the need for accurate biomechanical models that encapsulate the stress-strain response over a range of loads and dynamic time-scales.

Development of appropriate biomechanical models involves replicating experimental results in a manner that elucidates the link between the stresses and strains. Tissues exhibit a broad range of mechanical responses (see Fig. 1), and have resulted in the development of various experimental approaches to mechanical testing. Tensile tests are some of the earliest and most straightforward experiments to be performed, with deformations being imposed on tissue samples either uniaxially (most commonly) or biaxially [33, 60, 87]. Compression tests have also been employed, with compression being applied either uniformly on a sample [103], or through local indentation [80]. Simple shear [37] and torsional shear [9, 140] provide yet another mode of probing material response. Pure shear is the homogeneous non-rotational flattening of a body, in which the principal strains remain parallel to their respective principal stress axes during deformation. For an incompressible material,

this can be achieved by holding one side at constant length while stretching or compressing one of the two remaining sides. For small deformations, simple shear and pure shear differ by rotation [72], but this does not hold true for large deformations [104]. Beyond the mode of deformation, experiments can utilize different dynamic loading/unloading protocols, illustrating a tissue's response to frequency [74, 115] or relaxation behavior [44, 150]. Alternatively, a sample can be subjected to deformation under a constant load, which characterizes the creep behavior of a tissue [80, 116]. The observed behavior under these tests may be post-processed to describe the tissues response, informing the selection of an appropriate constitutive model.

Hyperelasticity has been widely investigated in biomechanical modeling for a range of tissues including but not limited to artery [45, 51, 66, 68], ligament and tendon [69, 131, 153], valve [85, 96, 113, 126], brain [20, 75, 98, 102], myocardium [8, 48, 64, 151], liver [28, 47, 123], and skin [3, 14, 57]. Since inception, the field has burgeoned with many different constitutive formulations including polynomial [95, 99], exponential [34, 43, 147], logarithmic [68, 139] and Ogden [109] forms (or some combination [28, 145]). A review of different hyperelastic constitutive model forms in biomechanics can be found in [67, 154]. However, despite evidence of viscoelasticity being observed since the early biomechanical works [43, 44, 87], it has been neglected in favor of hyperelastic only approaches due to focuses on quasi-static analysis, limitations in available experimental data, and computational considerations. While hyperelastic formulations have enabled studies of biomaterials, viscoelastic effects such as stress relaxation, creep, hysteresis, and variable frequency response are often ignored (Fig. 2). Viscoelastic modeling was first investigated by bringing together linear rheological elements that exhibit purely elastic or purely viscous behavior - springs and dashpots [87]. The simplest and earliest forms involve these two elements arranged in series - Maxwell model, or in parallel - Kelvin-Voigt model [27, 30, 38, 56, 100]. To match physiological responses, these models are extended with an increased number of rheological elements, *e.g.,* the standard linear (Zener) model or the generalized Maxwell model [124, 155, 159]. Extension of these linear models to nonlinear viscoelasticity has also been presented in the literature, following varying generalizations [11, 31, 58, 63, 65]. These viscoelastic formulations provide a foundation for accurately capturing the rate-dependent behaviors of tissues.

An alternative to classical approaches are the class of fractional viscoelastic models (see [91] (1D) and [41] (3D)). Here, the first order derivatives common to classical models are replaced with fractional time derivatives, enabling the rate-dependency of the model to transition between elastic and viscous. This change in differential operator also introduces a relaxation spectrum with rate responses reflective of the power-law behavior observed in tissues [61, 84, 90, 137]. Although this can be replicated using multiple branches in the generalized Maxwell model [155, 160], the fractional approach achieves this using a single fractional derivative order α. While these models pose more complexity in their use for numerical simulations, efficient numerical approaches have recently been introduced that enable use of fractional models for tissue modeling [160]. The potential for these models to effectively simulate rate response in tissues and the development effective computational tools make fractional models another practical resource for describing tissue behavior.

With these numerous options, selecting an appropriate viscoelastic model form can become challenging. Comparisons of classical and fractional viscoelastic models has been carried for specific applications, but systematic analysis for nonlinear materials across common tests remains unclear. A study by Parker et al. [111] focused on the suitability of various models for the use of elastography in soft tissues to investigate small strain rate response. Another recent study by Bonfanti et al. [17] reviewed the behavior of linear elements for
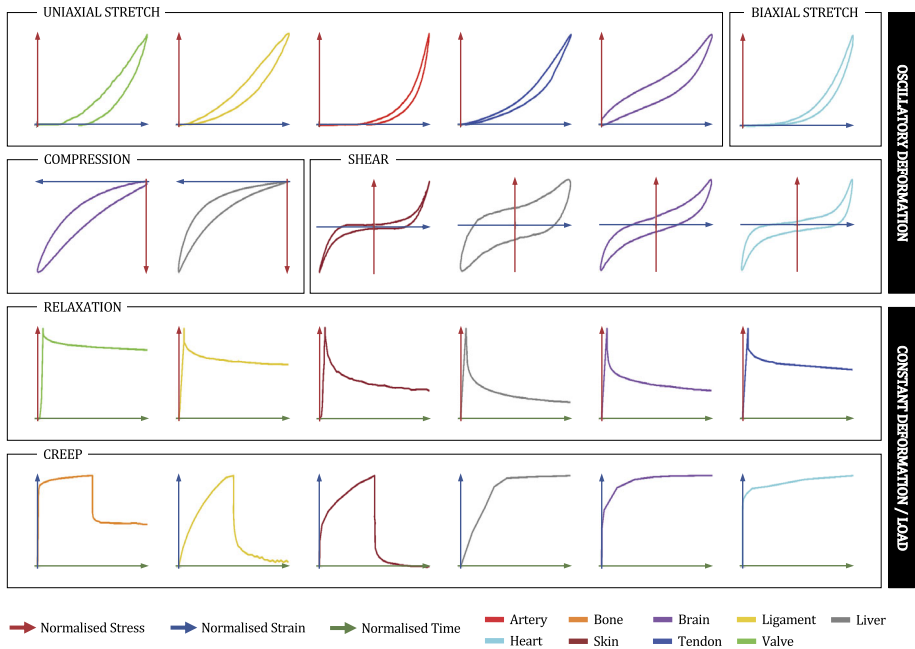
Fig. 2 Typical tissue behavior under various testing conditions, reproduced from literature sources: artery (uniaxial stretch [49]), bone (creep [92]), brain (uniaxial stretch, compression, shear and relaxation [21], creep [149]), ligament (uniaxial stretch [46], relaxation [120], creep [114]), liver (compression [73], shear [140]), relaxation [152], creep [12]), heart (biaxial stretch and shear [136], creep [116]), skin (shear [135], relaxation [76], creep [32]), tendon (uniaxial stretch [143], relaxation [71]), valve (uniaxial stretch [4], relaxation [36]). All data have been normalised, with maxima and minima reaching {1,0} or ±1, respectively, and the intersection point of axes denoting the origin (0, 0)

relaxation, creep and varying frequency response. Building on these studies to demonstrate the response of nonlinear materials across common rheological tests used in biomaterial modeling remains an important step for creating viscoelastic models.

In this work, we study a range of incompressible, isotropic and viscoelastic models across various testing protocols. The response of classical models (Maxwell, Kelvin-Voigt, Zener, generalized Maxwell) and their viscoelastic adaptions is investigated under oscillatory and long-term response (relaxation and creep) in uniaxial and biaxial stretch, compression, pure shear, as well as simple and torsional shear. We perform a methodical analysis on the impact of parameters on model behavior, with the aim of gaining an understanding on how these models can be employed and used to reproduce experimental data across a broad range of test conditions. This investigation enables a close look at these various viscoelastic forms and comparative analysis of their behaviors, providing a clear picture of how these models can be used to improve the modeling of tissue response.

This work is structured into several sections. Firstly, a brief review of fractional derivatives and kinematics is presented (Sect. 2.1, 2.2). The constitutive models are described in Sect. 2.3, starting from a basic exponential-type hyperelastic model extended to the classical and fractional viscoelastic approaches (Sect. 2.3-2.3.3). The kinematic characterization of the rheological tests considered follows in Sect. 2.4. Sect. 3 presents the analysis and interpretation of various combinations of viscoelastic model, testing protocol and parameters. The conclusions and key findings are summarised in Sect. 5.

2 Methods

In order to describe the behavior of various models across testing protocols, several technical aspects need to be clarified. Firstly, fractional derivatives and kinematics are briefly reviewed in Sect. 2.1-2.2. The viscoelastic modeling approach followed in this paper is described throughout Sect. 2.3, while the testing protocols are kinematically defined in Sect. 2.4. The parameter variations considered for each model across testing protocols is systematically presented in Sect. 2.4.3. Lastly, details on the numerical implementation of fractional derivatives and stress computation are explained in Sect. 2.5.

2.1 Review of Fractional Derivatives

We start by reviewing the concept of fractional derivatives, which is important to establishing the fractional viscoelastic models in later sections. Fractional calculus started with the generalization of integral and differential operators from the set of integers to the set of real numbers (for reviews, see, Ross [125] and Machado [89]). Many different definitions for fractional differential and integral operators of arbitrary order have been introduced [117], with the Caputo definition being a popular choice for physics-based applications. For a n-times differentiable function f and $0 < \alpha \leq n$, the Caputo derivative can be written as,

$$D_t^\alpha f = \frac{1}{\Gamma(\lceil \alpha \rceil - \alpha)} \int_0^t \frac{f^{\lceil \alpha \rceil}(s)}{(t-s)^{1+\alpha-\lceil \alpha \rceil}} ds, \tag{1}$$

where $\lceil \alpha \rceil$ denotes the ceiling of α and Γ is the Gamma function. For this work, we will only consider $0 \leq \alpha \leq 1$. The Caputo form (which can be related to other formulations like the Riemann-Louiville fractional derivative) has the advantage that

$$D_t^\alpha c = 0, \quad \text{for any constant } c \in \mathbb{R}. \tag{2}$$

The fractional derivative (for $\alpha \notin \mathbb{N}$), unlike integer derivatives, is a convolution of the past behavior of the function, making it particularly useful for incorporating the history of the stress of the material.

2.2 Review of Kinematics

To briefly review kinematics and kinetics in nonlinear mechanics [16, 63, 108, 130], let $\Omega_0 \subset \mathbb{R}^3$ denote the reference configuration of a three-dimensional solid and $\Omega(t) \subset \mathbb{R}^3$ denote its configuration at time t. At every time t, it is assumed that there exists a material displacement, $\mathbf{u} : \Omega_0 \times [0, T] \to \mathbb{R}^3$, relating the spatial position $\mathbf{x} \in \Omega(t)$ to the material position $\mathbf{X} \in \Omega_0$ by

$$\mathbf{x}(t) = \mathbf{u}(t) + \mathbf{X}, \qquad x_i(t) = u_i(t) + X_i, \tag{3}$$

where X_i and x_i denote the components of $\mathbf{X}$ and $\mathbf{x}$. We also assume that, due to the incompressible nature of the tissue, there exists a hydrostatic pressure $p : \Omega_0 \times [0, T] \to \mathbb{R}^3$ resisting volumetric change. This mapping in Eq. (3) is assumed to be bijective. The local deformation gradient $\mathbf{F}$ defining the mapping of Ω_0 to $\Omega(t)$ is given by

$$\mathbf{F} = \frac{\partial \mathbf{x}}{\partial \mathbf{X}} = \frac{\partial \mathbf{u}}{\partial \mathbf{X}} + \mathbf{I}, \qquad F_{ij} = \frac{\partial u_i}{\partial X_j} + \delta_{ij},$$

where $\mathbf{I}$ is the identity tensor. The determinant $J = \det \mathbf{F}$ defines the relative change in volume. The material stretch is characterized using $\mathbf{C}$ and $\mathbf{B}$, denoting the right and left Cauchy-Green tensors [63, 78], respectively, *e.g.,*

$$\mathbf{C} = \mathbf{F}^T \mathbf{F}, \qquad \mathbf{B} = \mathbf{FF}^T.$$

For isotropic hyperelastic biomechanical materials, the strain-energy function, $\Psi = \Psi(I_\mathbf{C}, II_\mathbf{C}, III_\mathbf{C})$, is often defined using three invariants of $\mathbf{C}$ [15],[1]

$$I_\mathbf{C} = \mathbf{C} : \mathbf{I}, \quad II_\mathbf{C} = \mathbf{C} : \mathbf{C}, \quad III_\mathbf{C} = \det \mathbf{C}.$$

From the second law of thermodynamics, the strain-energy function can be related to the second Piola-Kirchhoff stress tensor (PK2) as

$$\mathbf{S} = 2 \frac{\partial \Psi(\mathbf{C})}{\partial \mathbf{C}}, \qquad S_{ij} = 2 \frac{\partial \Psi(C_{ij})}{\partial C_{ij}}, \tag{4}$$

which, in turn, is related to the first Piola-Kirchhoff, $\mathbf{P}$, and the Cauchy stress tensors σ by push forward operations on $\mathbf{S}$,

$$\sigma = \frac{1}{J} \mathbf{FSF}^T = \frac{1}{J} \mathbf{PF}^T. \tag{5}$$

In what follows, we focus on constitutive forms of the second Piola-Kirchhoff stress, $\mathbf{S}$.

2.3 Constitutive Models of Viscoelastic Materials

In constitutive modeling of soft biological tissues it is common to express the hyperelastic stress in a material as the sum of the stress of its individual components (*i.e.,* $\mathbf{S}_e = \mathbf{S}_1 + \mathbf{S}_2...$). These may be stresses due to anisotropic structures [64, 66, 98], hydrostatic effects [51, 101, 138], or varying degrees of nonlinearity [28, 95, 99]. Similarly, it is also common to express the viscoelastic stress, $\mathbf{S}_{ve}$, as the sum of the elastic and viscous components. Letting $\mathbf{S}_e$ and $\mathbf{S}_Q$ denote some symmetric tensor form, then a simple viscoelastic model could be

$$\mathbf{S} = \mathbf{S}_{ve} - pJ\mathbf{C}^{-1}$$
$$\text{where} \quad \mathbf{S}_{ve} = \mathbf{S}_e + \frac{\partial \mathbf{S}_Q}{\partial t}. \tag{6}$$

$\mathbf{S}_e$ and $\mathbf{S}_Q$ are to be determined from the constitutive modeling of the tissue mechanical behavior and may or may not have the same form. While this encompasses models where elastic and viscous components are considered additive, a more generalized form can be written as

$$\mathbf{S} = \mathbf{S}_{ve} - pJ\mathbf{C}^{-1}$$
$$\text{where} \quad a_0 \mathbf{S}_{ve} + a_1 \frac{\partial \mathbf{S}_{ve}}{\partial t} = b_0 \mathbf{S}_e + b_1 \frac{\partial \mathbf{S}_Q}{\partial t}. \tag{7}$$

Here a's and b's denote specific model parameters that enable consideration of a wide range of models (discussed further below, see Fig. 4). In this case, the viscoelastic stress is defined

---

[1]Note that the second invariant $II_\mathbf{C}$ is defined as in Bonet and Wood [15], as opposed to the more common definition $II_\mathbf{C} = \frac{1}{2} I_\mathbf{C} - \mathbf{C} : \mathbf{C}$.

by a differential equation that must be solved (or approximated) to determine the current value of $\mathbf{S}_{ve}$, and is related to the elastic and viscous terms. Note that, the hydrostatic stress here is additive, and not encapsulated within the differential equation for $\mathbf{S}_{ve}$. This assumes that hydrostatic effects respond instantaneously without memory.

This form encapsulates many of the classical viscoelastic formulations. However, extending to greater generality, the differential operators can be replaced with fractional variants, giving the general form,

$$\mathbf{S} = \mathbf{S}_{ve} - p J \mathbf{C}^{-1}$$
$$\text{where} \quad a_0 \mathbf{S}_{ve} + a_1 D_t^{\alpha_a} \mathbf{S}_{ve} = b_0 \mathbf{S}_e + b_1 D_t^{\alpha_b} \mathbf{S}_Q, \tag{8}$$

where $D_t^{\alpha_a}$ denotes the Caputo derivative introduced in Eq. (1). Our main focus is to investigate different forms of $\mathbf{S}_{ve}$ in both classical ($\alpha_a, \alpha_b = 1$) and fractional approaches ($0 < \alpha_a, \alpha_b < 1$) and examine their viscoelastic behavior over a range of kinematic conditions. There are many variables to be considered: the constitutive model for the elastic component, $\mathbf{S}_e$; the constitutive model form for the viscous component, $\mathbf{S}_Q$; the non-linearity of the hyperelastic and viscoelastic component; and the weighting of terms based on different values of a's and b's.[2] The variations considered, along with theoretical comparisons, are outlined below and summarized in Table 1.

2.3.1 Constitutive Form of $\mathbf{S}_e$ and $\mathbf{S}_Q$

For the comparative analysis across viscoelastic models, we select a simple isotropic, exponential Fung-type model. Fung-type models are widely used in tissue modeling and their exponential form are versatile in capturing the behavior of various tissues in mechanical testing [44]. Here, we consider the specific form, $\mathbf{S}_{\text{fung}}(c_0, c_1, \mathbf{C})$, characterized by two parameters $c_0, c_1 \in \mathbb{R}^+$:

$$\mathbf{S}_{\text{fung}}(c_0, c_1, \mathbf{C}) = c_0 \exp\left(c_1(II_{\mathbf{C}} - 3)\right) \mathbf{C}. \tag{9}$$

In this stress definition, the parameter c_0 scales the stress-strain response, while c_1 enables varying degrees of nonlinearity. $\mathbf{S}_{\text{fung}}$ can be directly derived from the strain energy function $\Psi = \frac{c_0}{2c_1} \exp\left(c_1(II_{\mathbf{C}} - 3)\right)$ and was chosen based on previous experience. Other formulations could be considered, e.g., Mooney-Rivlin or Ogden-based forms as in Capilnasiu et al. [23]. However, the form used in Eq. (9) provides a good balance between model complexity and versatility. Further, we note that $\mathbf{S}_{\text{fung}}$ maintains symmetry and objectivity, which is particularly important when considering differential forms as in Eq. (8). Using this constitutive form, we set

$$\mathbf{S}_e = \mathbf{S}_{\text{fung}}(c_0^e, c_1^e, \mathbf{C}), \quad \mathbf{S}_Q = \text{dev}[\mathbf{S}_{\text{fung}}(c_0^v, c_1^v, \mathbf{C})], \tag{10}$$

with dev denoting the deviatoric operator, e.g. $\text{dev}[\mathbf{A}] = \mathbf{A} - \frac{1}{3}(\mathbf{A} : \mathbf{C})\mathbf{C}^{-1}$.[3] $\mathbf{S}_Q$ was chosen to have the same form as $\mathbf{S}_e$ to make it easier to interpret the extensive amount of results presented in the following sections. Given the generalized form shown in Eq. (8), we reduce

---

[2]Note for practical purposes, parameters a_0 and b_0 are set to 1, leading to a_1 and b_1 setting the relative contribution of $D_t^{\alpha_a}\mathbf{S}_{ve}$ and $D_t^{\alpha_b}\mathbf{S}_Q$, respectively.

[3]Note that the deviatoric form of $\mathbf{S}_Q$ was used for convenience to ensure that $\mathbf{S}_Q = \mathbf{0}$ when the body is unloaded and when prior strain history cannot be established at the start of the simulations.

Table 1 Table of (top) classic and (bottom) fractional viscoelastic models, highlighting the analogue between linear and nonlinear forms. Here, the relaxation modulus for the linear and nonlinear forms is given by $\mathcal{K}_{\ell,n}(s,t) = \sum_{k=1}^{n} E_k \exp\{\frac{s-t}{\tau_k}\}$ and $\mathcal{K}_n(s,t) = \sum_{k=1}^{n} b_k \exp\{\frac{s-t}{\tau_k}\}$, respectively

CLASSIC VISCOELASTIC MODELS

Model	Equation			Parameter analogues
Maxwell	Lin	$\sigma + \frac{\eta_1}{E_1}\dot{\sigma} = \eta_1\dot{\varepsilon}$		$a_1 \sim \eta_1/E_1$
	Nonlin	$\mathbf{S}_{ve} + a_1\dot{\mathbf{S}}_{ve} = b_1\dot{\mathbf{S}}_Q$		$b_1 \sim \eta_1$
Kelvin-Voigt	Lin	$\sigma = E_0\varepsilon + \eta_1\dot{\varepsilon}$		$b_0 \sim E_0$
	Nonlin	$\mathbf{S}_{ve} = b_0\mathbf{S}_e + b_1\dot{\mathbf{S}}_Q$		$b_1 \sim \eta_1$
Zener SLS	Lin	$\sigma + \frac{\eta_1}{E_1}\dot{\sigma} = E_0\varepsilon + \eta_1\frac{E_0+E_1}{E_1}\dot{\varepsilon}$		$a_1 \sim \eta_1/E_1$
	Nonlin	$\mathbf{S}_{ve} + a_1\dot{\mathbf{S}}_{ve} = b_0\mathbf{S}_e + b_1\dot{\mathbf{S}}_Q$		$b_0 \sim E_0$ $b_1 \sim \eta_1(1 + \frac{E_0}{E_1})$
Zener SLS *integral form*	Lin	$\sigma(t) = E_0\varepsilon(t) + \int\limits_0^t (E_0 + \mathcal{K}_{\ell,1}(s,t))\dot{\varepsilon}(s)\,\mathrm{d}s$		$b_0 \sim E_0$ $\tau_1 \sim \eta_1/E_1$
	Nonlin	$\mathbf{S}_{ve}(t) = b_0\mathbf{S}_e(t) + \int\limits_0^t \mathcal{K}_1(s,t)\dot{\mathbf{S}}_Q(s)\,\mathrm{d}s$		$b_1 \sim E_0 + E_1$
Generalized Maxwell *integral form*	Lin	$\sigma(t) = E_0\varepsilon(t) + \int\limits_0^t \mathcal{K}_{\ell,n}(s,t)\dot{\varepsilon}(s)\,\mathrm{d}s$		$b_0 \sim E_0$ $b_k \sim E_k/E_0$
	Nonlin	$\mathbf{S}_{ve}(t) = b_0\mathbf{S}_e(t) + \int\limits_0^t \mathcal{K}_n(s,t)\dot{\mathbf{S}}_Q(s)\,\mathrm{d}s$		

FRACTIONAL VISCOELASTIC MODELS

Model	Equation			Parameter analogues
Fractional Maxwell	Lin	$\sigma + \frac{\eta_1}{E_1}D_t^\alpha\sigma = \eta_1 D_t^\alpha\varepsilon$		$a_1 \sim \eta_1/E_1$
	Nonlin	$\mathbf{S}_{ve} + a_1 D_t^\alpha\mathbf{S}_{ve} = b_1 D_t^\alpha\mathbf{S}_Q$		$b_1 \sim \eta_1$
Fractional Kelvin-Voigt	Lin	$\sigma = E_0\varepsilon + \eta_1 D_t^{\alpha_b}\varepsilon$		$b_0 \sim E_0$
	Nonlin	$\mathbf{S}_{ve} = b_0\mathbf{S}_e + b_1 D_t^{\alpha_b}\mathbf{S}_Q$		$b_1 \sim \eta_1$
Fractional Zener	Nonlin	$\mathbf{S}_{ve} + a_1 D_t^{\alpha_a}\mathbf{S}_{ve} = b_0\mathbf{S}_e + b_1 D_t^{\alpha_b}\mathbf{S}_Q$		

redundancy by setting $c_0^e = c_0^v = 1$. Moreover, while in general c_i^e and c_i^v may be selected arbitrarily, to reduce space of potential models, we chose these parameters to be equivalent for elastic and viscous tensor components.

2.3.2 Classical Viscoelastic Model Examples

This section focuses on classical viscoelastic models that are often encountered in literature. These models are summarised in Table 1 and are separated into their formal linear and non-linear forms. The nonlinear analogues provide a form corresponding to the same modeling approach as the linear models but do not necessarily equate in the linear viscoelastic limit. To maintain object reference, the Cauchy stress σ is replaced by the PK2 tensor, $\mathbf{S}_{ve}$, in the nonlinear analogue. In the classical form, elastic contributions are replaced by $\mathbf{S}_e$ and viscous contributions by $\mathbf{S}_Q$. For the classical forms, $\alpha_a, \alpha_b = 1$ in Eq. (8) as shown in Eq. (7).
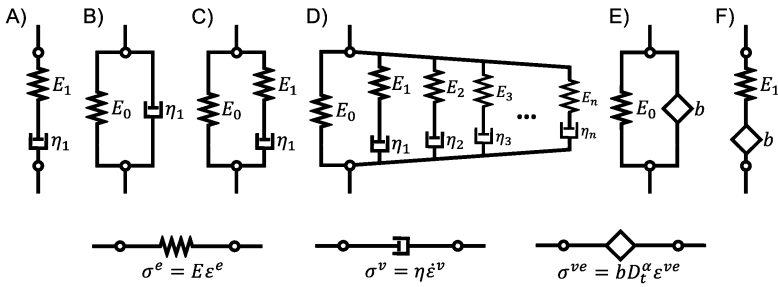
Fig. 3 Common viscoelastic models based on arrangements of spring, dashpot and spring-pot elements: **A)** Maxwell, **B)** Kelvin-Voigt, **C)** Standard Linear (Zener), **D)** Generalized Maxwell, **E)** Fractional Kelvin-Voigt, **F)** Fractional Maxwell. The linear spring, dashpot and spring-pot are defined in the lower row

The first classical form in this study is based on the Maxwell model, composed of a spring and dashpot in series (see Fig. 3 A). The nonlinear formulation of the model, given below, represents a simplified differential form for $\mathbf{S}_{ve}$ where

$$\mathbf{S}_{ve} + a_1 \frac{\partial \mathbf{S}_{ve}}{\partial t} = b_1 \frac{\partial \mathbf{S}_Q}{\partial t}. \tag{11}$$

Recall that $\mathbf{S}_Q$ is defined as in Eq. (10). The model can be tuned through three parameters: a_1, b_1, and c_1^v, where a_1 and b_1 scale linearly the time derivative of $\mathbf{S}_{ve}$ and $\mathbf{S}_Q$, respectively, and c_1^v scales the exponential power in Eq. (9). The Maxwell model is particularly useful in modeling relaxation behavior, but is known to be unable to predict typical creep behavior [100]. When held under constant stress, materials usually exhibit creep that gradually slow to a stop. However, this model displays a linear strain increase (constant rate).

An alternate form is the arrangement in parallel of a spring and dashpot, known as the Kelvin-Voigt model (see Fig. 3 B). Here,

$$\mathbf{S}_{ve} = \mathbf{S}_e + b_1 \frac{\partial \mathbf{S}_Q}{\partial t}. \tag{12}$$

$\mathbf{S}_e$ and $\mathbf{S}_Q$ are defined as in Eq. (10), with the exponential parameters $c_1^{e,v}$ controlling the nonlinearity of the model. Parameter b_1 acts as linear scaling factor, leading to a total of three parameters to tune the model. The Kelvin-Voigt model has the advantage that it can model creep behavior, but inherently it cannot predict stress relaxation. Instantaneous drop in velocity will result in an instantaneous drop in stress, whereas an exponential decay is normally observed in tissues (see Fig. 2).

The standard linear solid model, also known as the Zener model, combines two springs and a dashpot. One possible arrangement is having a spring in series with a Kelvin-Voigt configuration or, as considered here, having a spring in parallel to a Maxwell configuration, as shown in Fig. 3 C. In this configuration, the nonlinear Zener model becomes

$$\mathbf{S}_{ve} + a_1 \frac{\partial \mathbf{S}_{ve}}{\partial t} = \mathbf{S}_e + b_1 \frac{\partial \mathbf{S}_Q}{\partial t}. \tag{13}$$

As before, $\mathbf{S}_{ve}$, $\mathbf{S}_e$ and $\partial \mathbf{S}_Q/\partial t$ are the viscoelastic, elastic and viscous PK2 stresses, respectively. Four parameters are used to describe the model. Firstly, $c_1^{e,v}$ scale the exponential power and thus have a nonlinear influence on the model, while a_1 and b_1 act as linear scaling factors. By having a more complex arrangement of rheological elements, both in

series and in parallel, the Zener model bypasses the issues encountered by the Maxwell and Kelvin-Voigt models in creep and relaxation, respectively.

Another development of classical rheological models is the generalized Maxwell model with n branches, as depicted in Fig. 3 D. Note that the Zener model is a particular form of the Generalized Maxwell model with only one branch. The benefit of having multiple branches is that they allow for a more diverse set of rate responses within the model, enabling a more tailored relaxation response [1, 127, 128]. For compactness, this model is presented below in its integral form, as

$$\mathbf{S}_{ve}(t) = \mathbf{S}_e(t) + \int_0^t \sum_{k=1}^n b_k \exp\{(s-t)/\tau_k\} \frac{\partial \mathbf{S}_Q(s)}{\partial s} \, ds. \tag{14}$$

A total of $2n + 2$ parameters are needed in this case. Firstly, the exponential power scales $c_1^{e,v}$ trigger a nonlinear response in the formulation of the PK2 stresses $\mathbf{S}_e$ and $\mathbf{S}_Q$. Then, each branch is defined by the relaxation time τ_k and relaxation weight b_k. The generalized Maxwell model is the most comprehensive classical viscoelastic model, providing flexibility in representing decaying relaxation spectra. However, this generality comes at the added cost of an increased number of parameters.

2.3.3 Fractional Viscoelastic Models

Fractional models provide an alternative to classical models in modeling viscoelasticity. From a rheological standpoint, a fractional element can be imagined as a spring-pot, analogous to a more complex set of Maxwell elements arranged in parallel [160]. Thus, it is functionally similar to Eq. (14) with pre-established weights and decay constants that are not free parameters, but tied to the underlying fractional order. This is achieved using the fractional derivative (Eq. (1)) with the order $0 < \alpha < 1$. As in the case of the classical models, the fractional models discussed here are summarised in Table 1. There, the linear form of the models is provided, alongside the nonlinear analogues which are further presented in this section.

The first fractional model considered here will be referred to as the fractional Kelvin-Voigt, which provides a direct alternative to the generalized Maxwell model. The nonlinear fractional Kelvin-Voigt model is described by
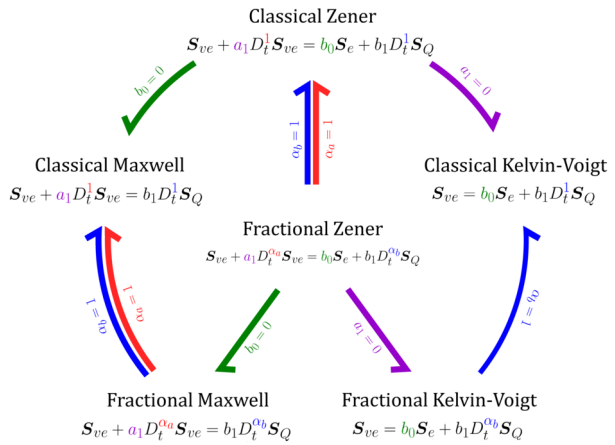
$$\mathbf{S}_{ve} = \mathbf{S}_e + b_1 D_t^{\alpha_b} \mathbf{S}_Q. \tag{15}$$

Note the similitude between the fractional and classical Kelvin-Voigt models shown in Eqs. (15) and (12). If the fractional order is chosen such that $\alpha_b = 1$, then Eq. (12) is recovered, but the benefits of the fractional model are lost and relaxation issues arise. This is because, as α_b increases, the relaxation spectrum of the model increasingly weights more recent events over the past. Overall, the fractional Kelvin-Voigt model captures the same complexity as the generalized Maxwell model (with preset assumptions about the distribution of the spectra) and uses four parameters - the scaling parameters b_1, the exponential scaling powers $c_1^{e,v}$ and the fractional order α_b.

Another fractional model analogue to a classical configuration is the fractional Maxwell model. This is derived by replacing the dash-pot with a spring-pot, leading to a series configuration as seen in Fig. 3 F. Following the form shown in the classical Maxwell (Eq. (11)), the fractional version replaces full derivatives with fractional counterparts, *e.g.,*

$$\mathbf{S}_{ve} + a_1 D_t^{\alpha_a} \mathbf{S}_{ve} = b_1 D_t^{\alpha_b} \mathbf{S}_Q. \tag{16}$$

Fig. 4 Interrelation of fractional and classical viscoelastic formulations for Maxwell, Kelvin-Voigt, and Zener model variants. The diagram shows how selection of specific parameters in the fractional Zener model can result in all model forms

Classical Zener

$$\boldsymbol{S}_{ve} + a_1 D_t^1 \boldsymbol{S}_{ve} = b_0 \boldsymbol{S}_e + b_1 D_t^1 \boldsymbol{S}_Q$$

Classical Maxwell

$$\boldsymbol{S}_{ve} + a_1 D_t^1 \boldsymbol{S}_{ve} = b_1 D_t^1 \boldsymbol{S}_Q$$

Classical Kelvin-Voigt

$$\boldsymbol{S}_{ve} = b_0 \boldsymbol{S}_e + b_1 D_t^1 \boldsymbol{S}_Q$$

Fractional Zener

$$\boldsymbol{S}_{ve} + a_1 D_t^{\alpha_a} \boldsymbol{S}_{ve} = b_0 \boldsymbol{S}_e + b_1 D_t^{\alpha_b} \boldsymbol{S}_Q$$

Fractional Maxwell

$$\boldsymbol{S}_{ve} + a_1 D_t^{\alpha_a} \boldsymbol{S}_{ve} = b_1 D_t^{\alpha_b} \boldsymbol{S}_Q$$

Fractional Kelvin-Voigt

$$\boldsymbol{S}_{ve} = b_0 \boldsymbol{S}_e + b_1 D_t^{\alpha_b} \boldsymbol{S}_Q$$

Five parameters define the model: the linear scaling factors a_1 and b_1, the fractional orders α_a and α_b and the exponential power scaling c_1^v. For non-extreme α_a, α_b values (*i.e.,* $\alpha_a, \alpha_b < 1$), the fractional Maxwell model may change in the creep description, but this response will be investigated later in this study.

Lastly, here we devise a comprehensive fractional model that combines the fractional Kelvin-Voigt and Maxwell formulations, with the liberty of having a different fractional order derivative of the total viscoelastic stress $\boldsymbol{S}_{ve}$ and the viscoelastic stress $\boldsymbol{S}_Q$. In this case,

$$\boldsymbol{S}_{ve} + a_1 D_t^{\alpha_a} \boldsymbol{S}_{ve} = \boldsymbol{S}_e + b_1 D_t^{\alpha_b} \boldsymbol{S}_Q, \tag{17}$$

which will be referred to as the fractional Zener model. Here, six parameters are needed for the model: the fractional orders α_a and α_b, the linear scaling terms a_1, b_1, and the exponential power parameters $c_1^{e,v}$. This is the most general model form, from which the other models can be obtained (see Fig. 4), *e.g.,* the nonlinear fractional Maxwell by disregarding the $\boldsymbol{S}_e$ contribution (*i.e.,* setting b_0 to 0), or even the classical form by additionally setting $\alpha_a = \alpha_b = 1$. The transformation to the generalized Maxwell model is not immediately obvious. However, by recalling that the nonlinear fractional Kelvin-Voigt is an alternative approximation to the generalized Maxwell model, then setting $a_1 = 0$ provides the correspondence.

2.4 Common Biomechanical Testing Paradigms

To examine the capacity of the different classical and fractional viscoelastic models to exhibit realistic behaviors, a series of common biomechanical testing paradigms were considered. While there are numerous testing protocols in the literature, this work focused on strain loading cases, including uniaxial extension/compression, biaxial extension (with pure shear as a special case), simple shear, and torsion, as well as stress loading such as creep. To capture viscoelastic responses, different modes of cyclic (with varying frequency) or static loading were also considered.

2.4.1 Dynamics of Strain and Stress Loading

The impact of viscoelasticity on the mechanical function of biological tissues and organs can be divided into the short and long-term responses. *In vivo* periods of short-term cyclic

loading (*e.g.,* pulsation due to flow, breathing, walking, etc) and long-term static loading (*e.g.,* diastolic blood pressure, standing, sitting, sleeping, etc) can be observed. As a consequence, experimental rheological studies have been designed to probe a broad range of tissue responses. Capturing both cyclic and static responses, we introduce three primary dynamic functions, covering common dynamics used in rheological experiments,

$$a_{\sin}(t, \tau_P) = \sin\left(\frac{2\pi t}{\tau_P}\right),$$

$$a_{\text{saw}}(t, \tau_P) = \frac{2}{\pi}\sin^{-1}(a_{\sin}(t, \tau_P)), \tag{18}$$

$$a_{\text{step}}(t, \tau_P) = \max\left\{0, \min\left\{1, \frac{5}{2}\left(0.2 + a_{\text{saw}}(t, \tau_P)\right)\right\}\right\},$$

denoting sinusoidal temporal variations, sawtooth variations and periodic step functions. Here, τ_P denotes the period of oscillation, which can be extended for long-term static loading. Note that dynamic functions are bounded in time, *e.g.,* $|a_k(t)| \in [0, 1]$, $\forall t \in \mathbb{R}$. Further, a_{step} is introduced whereby 10% of the period is spent ramping up or down the load, 40% of the period spent statically holding the load, and 40% of the period spent recording recovery.

In this paper, we consider both strain loading and stress loading. Focusing initially on strain loading, we consider both stretch and shear. Using the dynamic function of Eq. (18), the stretch, λ, and shear, γ, can be defined as,

$$\lambda_k(t, \tau_P) = 1 + (\lambda^{\max} - 1)a_k(t, \tau_P), \qquad \gamma_k(t, \tau_P) = \gamma^{\max}a_k(t, \tau_P). \tag{19}$$

Here $\lambda^{\max}$ denotes the maximal stretch or shear achieved.

Stress loading is also applied in the literature, whereby a preset force is prescribed and the material stretch or shear is recorded. In this paper, we focus on creep response, in which a certain set load, T, is applied to the material and released, *i.e.,*

$$T(t, \tau_P) = T^{\max}a_{\text{step}}(t, \tau_P). \tag{20}$$

Here τ_P denotes the period of on/off loading and unloading, and $T^{\max}$ denotes the total load applied. In this work, only step loading is considered, reflective of the typical dynamics applied in the literature. The following sections outline the kinematics applied in strain loading. In this case, the stretch, λ, and shear, γ are referred to without parameters or superscripts for ease.

2.4.2 Kinematics of Simple Deformations

This work focuses on the viscoelastic response of models to the 4 pure deformation kinematics, uniaxial, biaxial, simple shear, and torsion. The isotropic nature of the mechanical response considered removes the need for consideration of different loading directions, reducing the number of kinematic variants considered. For uniaxial deformation, we will examine both the tensile and compressive cases, where the deformation gradient in vector notation is given by

$$\mathbf{F} = \lambda_1(t)\mathbf{e}_1 \otimes \mathbf{e}_1 + \frac{1}{\sqrt{\lambda_1(t)}}\left(\mathbf{e}_2 \otimes \mathbf{e}_2 + \mathbf{e}_3 \otimes \mathbf{e}_3\right), \tag{21}$$

where λ_1 denotes the applied stretch or compression (applied in the $\hat{e}_1$ direction). The biaxial deformation will be restricted to a general case, where $\lambda_2 > \lambda_1$, and pure shear. Biaxial deformation in general is given by

$$\mathbf{F} = \lambda_1(t)\mathbf{e}_1 \otimes \mathbf{e}_1 + \lambda_2(t)\mathbf{e}_2 \otimes \mathbf{e}_2 + \frac{1}{\lambda_1(t)\lambda_2(t)}\mathbf{e}_3 \otimes \mathbf{e}_3, \tag{22}$$

where one definition of pure shear can be expressed as

$$\mathbf{F} = \lambda_1(t)\mathbf{e}_1 \otimes \mathbf{e}_1 + \frac{1}{\lambda_1(t)}\mathbf{e}_2 \otimes \mathbf{e}_2 + \mathbf{e}_3 \otimes \mathbf{e}_3, \tag{23}$$

which is more commonly found in experimental studies as it is much simpler to be applied mechanically [104]. For testing the mechanical response under shear, we consider mainly the simple shear case given by

$$\mathbf{F} = \gamma_1(t)\mathbf{e}_1 \otimes \mathbf{e}_2 + \mathbf{I}. \tag{24}$$

Torsion testing is a common method for probing the viscoelastic properties of 3-dimension tissues (where the membrane assumption is not applicable). Here a block or more commonly a disk of tissue is placed between a stationary plate and a linear actuator. An initial small compressive load is first applied and then the actuator will twist cyclically at a predetermined frequency. The deformation applied consists of both compressive and extensional loading as well as shearing, and the deformation applied is also heterogenous, as it shears more away from the central axis of the tissue. Simulating the torsion testing is thus a good example application to examine the mechanical response of the viscoelastic model forms.

We do note that the method of attachment is a complex issue and the deformation exhibited is often non-ideal (*i.e.,* the deformed tissue will bulge at the middle). Our goal is not to replicate the full experimental setup and will as such assume ideal deformations, *i.e.,* the geometry of the tissue will remain perfectly cylindrical. The deformation gradient for such a setup is given by

$$\Theta(X_3, t) = \frac{\lambda_z^{3/2}}{R}\gamma(t)X_3$$

$$\begin{aligned} \mathbf{F}(t) = {}& \frac{1}{\sqrt{\lambda_z}}\cos\Theta(X_3, t)\mathbf{e}_1 \otimes \mathbf{e}_1 - \frac{1}{\sqrt{\lambda_z}}\sin\Theta(X_3, t)\mathbf{e}_1 \otimes \mathbf{e}_2 \\ & + \frac{1}{\sqrt{\lambda_z}}\sin\Theta(X_3, t)\mathbf{e}_2 \otimes \mathbf{e}_1 + \frac{1}{\sqrt{\lambda_z}}\cos\Theta(X_3, t)\mathbf{e}_2 \otimes \mathbf{e}_2 \\ & - \frac{\lambda_z}{R}\gamma(t)\left(X_1\sin\Theta(X_3, t) + X_2\cos\Theta(X_3, t)\right)\mathbf{e}_1 \otimes \mathbf{e}_3 \\ & + \frac{\lambda_z}{R}\gamma(t)\left(X_1\cos\Theta(X_3, t) - X_2\sin\Theta(X_3, t)\right)\mathbf{e}_2 \otimes \mathbf{e}_3 \\ & + \lambda_z\mathbf{e}_3 \otimes \mathbf{e}_3, \end{aligned} \tag{25}$$

where γ is the shear applied by the twisting angle Θ, R is the initial radius of the specimen, and λ_z is the initial compressive loading applied.

2.4.3 Classical and Fractional Viscoelastic Model Analysis

In order to understand the envelope of behavior for each model, simulations were performed across all testing paradigms using varying model parameters. As previously mentioned, parameters c_0^e and c_0^v were set to 1, to avoid redundancy with the b_0 and b_1 parameters. The exponential parameters, $c_1^e = c_1^v = c_1$, were set to be equal for simplicity. Without loss of generality, parameter a_0 is set to 1 (Eq. (8)). For analysis purposes, the elastic part parameter b_0 was also set to 1 (for the Zener and Kelvin-Voigt forms) or zero (for the Maxwell model forms). While changing b_0 alters the material response, it can be shown that the behavior can be replicated with a $b_0 = 1$, re-weighting of a_1 and b_1, and a scaling of the total stress response (except in the case where $b_0 = 0$). In our analysis, we focus on comparing normalized stresses/strains (*i.e.,* divided by their respective maximum value, which after normalization becomes 1), simplifying the need to consider all three parameters. Following the same reason, $b_1 = 1$ for all Maxwell model forms.

As a result, a_1 and b_1 become the principal scaling parameters responsible for the relative contribution of the viscoelastic components. Below we list the parameter variations considered in this analysis:

– $a_1 \in \{0.01, 0.02, 0.05, 0.1, 0.2, 0.3, 0.5, 0.8\}$
– $b_1 \in \{0.2, 0.5, 1, 2, 5, 20\}$
– $c_1 \in \{0.5, 1, 2, 5\}$
– $\alpha_a \in \{0.1, 0.2, 0.5, 0.8\}$
– $\alpha_b \in \{0.1, 0.2, 0.5, 0.8\}$

As shown in Fig. 4, here we consider the Classical Maxwell (varying a_1 and c_1, resulting in 32 models), Classical Kelvin-Voigt (varying b_1 and c_1, resulting in 24 models), Classical Zener (varying a_1, b_1 and c_1, resulting in 192 models), Fractional Maxwell (varying a_1, c_1, α_a and α_b, resulting in 512 models), Fractional Kelvin-Voigt (varying b_1, c_1, α_a and α_b, resulting in 384 models) and Fractional Zener (varying a_1, b_1, c_1, α_a and α_b, resulting in 3, 072 models). The generalized Maxwell model is not explicitly included in the analysis as the generality of the model makes it more difficult to compare across all possible parameter variations.

Examining model behaviors, we aimed to address model responses for varying testing paradigms. Each testing paradigm includes the variation of kinematics, load level, cycling period, and cycling wave function. The kinematics include uniaxial, biaxial, pure shear, simple shear, torsion, uniaxial relaxation, and uniaxial creep. The loading parameter for each testing paradigm varies as following

– Uniaxial: $\lambda_1^{\max} \in \{1.05, 1.1, 1.2, 1.4\}$,
– Biaxial: $(\lambda_1^{\max}, \lambda_2^{\max}) \in \{(1.05, 1.075), (1.1, 1.5), (1.2, 1.3), (1.4, 1.6)\}$
– Pure shear: $\lambda_1^{\max} \in \{1.05, 1.1, 1.2, 1.4\}$
– Simple shear & torsion: $\gamma^{\max} \in \{0.05, 0.1, 0.2, 0.4\}$
– Relaxation: $\lambda_1^{\max} \in \{1.05, 1.1, 1.2, 1.4\}$
– Creep: $T^{\max} \in \{1, 10, 100, 1000\}$ kPa

Uniaxial, biaxial, pure shear, simple shear, and torsion tests were ran with sinusoidal and sawtooth wave functions ($a_{\sin}$ and a_{saw} in Eq. (18)) for cycling periods of $\tau_p = 0.2$ s (5 Hz), 2 s (0.5 Hz), and 20 s (0.05 Hz). Relaxation and creep both used the a_{step} wave function with periods of $\tau_P = 0.5$ s, 5 s, and 50 s. In total, 144 tests were examined: 24 for uniaxial, biaxial, pure shear and simple shear, as well as 12 for both relaxation and creep. Performing each of the 144 tests across the 4, 216 models resulted in 607, 104 model outputs.

For the uniaxial case, a frequency sweep of the dynamic tensile modulus at small strains (1%) was also conducted. Here, frequencies of 10^{-3}, 10^{-2}, 10^{-1}, 1, 10^1, 10^2, 10^3, 5×10^{-3}, 5×10^{-2}, 5×10^{-1}, 5, 5×10^1, and 5×10^2 Hz were calculated. Loading was applied using the sinusoidal wave with $\lambda^{\max} = 1.01$ and the nonlinearity of the model was chosen to be $c_1 = 0.5$. Only uniaxial deformation is considered due to the limited range of strain and the nonlinearity of the model. For determining the storage and loss moduli over 10^{-3} to 10^3 Hz, the stress and strain responses were fit to a sine function on the 5th oscillatory cycle. The Cauchy stress over time, σ, and strain over time, ϵ, were fit to

$$\sigma(t) = \sigma_0 \sin(\omega t + \delta_\sigma), \qquad \epsilon(t) = \epsilon_0 \sin(\omega t + \delta_\epsilon), \tag{26}$$

using the optimization library from Mathematica [157] (where $\omega = 2\pi/\tau_P$). Following Meyers and Chawla [100], the storage and loss moduli were computed as

$$E' = \frac{\sigma_0}{\epsilon_0} \cos(\delta_\sigma - \delta_\epsilon), \qquad E'' = \frac{\sigma_0}{\epsilon_0} \sin(\delta_\sigma - \delta_\epsilon). \tag{27}$$

Due to the significant amount of data available, we present the data analysis by focusing on outliers and the best case parameters for each model form. We devised an approach by computing a similarity metric between the models, examining how this metric varies with different model forms and parameters with a focus on the worst values. Given that all existing data was simulated, the sum of the residual squared is used to measure the difference between two curves. This value was then normalized by the mean total variance between the two curves. Thus, the metric is given by

$$\mu = \frac{\sum_i 2 \left(f_1(t_i) - f_2(t_i)\right)^2}{\sum_i \left(f_1^2(t_i) + f_2^2(t_i)\right)}, \tag{28}$$

where f_i is the curve of the normalized stress or strain component (by maximum positive value), respectively. For each kinematic, load magnitude, loading frequency, and material nonlinearity, we first compared how similar each pair of model forms is, to get an overview of model responses under the tested conditions. While this examination provides insight into contrasting or similar behaviors in models, it does not capture whether models exhibit physical behavior, such as those seen in Fig. 2. To get an impression about this, a representative response was selected from the Fractional Zener models that exhibited realistic responses under the different testing modes. All other models were then examined to find which best matched the exhibited response, providing a way of determining whether physically reasonable responses were viable for a given model. Given what was observed, we focused on presenting the result in terms of the overall similarity patterns and best case results for the kinematics, loading level, and frequency response.

2.5 Numerical Approximation of Model Responses

The above examples were implemented and simulated using Python3 (Python Software Foundation, https://www.python.org/). The strain loading tests were straightforward to implement using the NumPy library for support of array operations [110, 144]. The fractional derivative were computed using the Prony series method [160]. To summarize, this approach is equivalent to using N Maxwell elements arranged in parallel, each with their own stiffness β_k and time constant τ_k ($k = 1 \ldots N$), chosen to optimally approximate the fractional derivative for a given order. Supposing we wish to take the α-order fractional derivative

($\alpha \in [0, 1]$) of the temporal tensor function $\mathbf{A} : [0, T] \to \mathbb{R}^{3 \times 3}$ at any time $t \in [0, T]$, then the Prony series approximation to the true Caputo derivative in Eq. (1) can be written as

$$\hat{D}_t^\alpha \mathbf{A} := \beta_0 \mathbf{A}'(t) + \sum_{k=1}^N \mathbf{Q}_k(t), \quad \mathbf{Q}_k'(t) + \frac{1}{\tau_k} \mathbf{Q}_k(t) = \beta_k \mathbf{A}'(t), \tag{29}$$

where $\mathbf{Q}_k : [0, T] \to \mathbb{R}^{3 \times 3}$ is an introduced intermediate variable corresponding to the kth Maxwell element. Discretization of $\hat{D}_t^\alpha$ was accomplished applying standard backward Euler. The resulting discrete approximation at $t_n = n\Delta_t$, denoted as $\hat{D}_n^\alpha$, can be written as

$$\hat{D}_n^\alpha \mathbf{A} := \beta_0 \frac{\mathbf{A}^n - \mathbf{A}^{n-1}}{\Delta_t} + \sum_{k=1}^N \mathbf{Q}_k^n, \quad \mathbf{Q}_k^n = e^{-\frac{\Delta_t}{\tau_k}} \mathbf{Q}_k^{n-1} + \beta_k e^{-\frac{\Delta_t}{2\tau_k}} \left(\mathbf{A}^n - \mathbf{A}^{n-1} \right). \tag{30}$$

Here the computational cost stays constant over time and the storage of historical values is limited to the size of $\mathbf{A}^{n-1}$ and $\mathbf{Q}_k^{n-1}$ (for each $k = 1, \ldots N$). Applied to Eq. (8), the fractional operator must be applied to both $\mathbf{S}_{ve}$ and $\mathbf{S}_Q$. For test cases when the temporal dynamics of $\mathbf{S}_Q$ were known, we note that the backward Euler derivative in Eq. (30) was computed using a more accurate approximation (using central difference with $h = \max(\lambda, 1)(\epsilon^{1/3})$ where ϵ is the machine epsilon for double precision numbers). After isolating the correct terms, the stresses at the nth step are calculated using

$$\mathbf{S}_{ve}^n = \frac{\mathbf{S}_e^n + b_1 \hat{D}_n^{\alpha_b} \mathbf{S}_Q - a_1 \sum_{k=1}^N e^{-\frac{\Delta t}{\tau_k}} \mathbf{Q}_k^{n-1} + a_1 \left(\frac{\beta_0}{\Delta t} + \sum_{k=1}^N \beta_k e^{-\frac{\Delta t}{2\tau_k}} \right) \mathbf{S}_{ve}^{n-1}}{1 + a_1 \left(\frac{\beta_0}{\Delta t} + \sum_{k=1}^N \beta_k e^{-\frac{\Delta t}{2\tau_k}} \right)}. \tag{31}$$

The heterogeneity in strain for the torsion example (Eq. (25)) requires the computation of the stresses over the top surface of which the traction is applied. Taking into consideration the observations from Mazzia et al. [97], the stresses were computed at quadrature point on a disk determined using the Gauss-Legendre rule in r ($n = 8$) and mid-point rule in θ ($n = 8$). For these series of tests, Δ_t was chosen to be 0.01 times the period of one loading cycle.

For the uniaxial creep simulations, a forward simulation was not possible due to the combination of applied tension, incorporation of strain history and solving of the differential equation Eq. (8). Instead, at each time step, an inverse problem had to be solved whereby the applied traction (see Eq. (20)), $T\mathbf{e}_1$, on the surface with normal $\mathbf{e}_1$, had to balance with the stress at an unknown stretch, λ_1, e.g.,

$$T\mathbf{e}_1 - J\mathbf{F}\mathbf{S}(\lambda_1)\mathbf{F}^T \cdot \mathbf{e}_1 = \mathbf{0}. \tag{32}$$

Without a defined $\lambda_1(t)$, $\frac{\partial \mathbf{S}_Q}{\partial t}$ in $D_t^{\alpha_b} \mathbf{S}_Q$ (Eq. (8)) was also computed implicitly by backwards Euler. Solving for λ_1 was numerically unstable for some of the classical forms with larger time steps, where convergence was not consistently achievable with Newton-Raphson iterations. Taking into account the time and data storage due to the number of simulations being ran, dt was chosen to be 0.005 times the period of one cycle and a more rigorous 2 layered approach was taken for solving Eq. (32), with Brent's method [19] initially and a differential evolution step if Brent's method fails. For Brent's method, the λ_1^{n-1} was taken as one bound of the initial condition. The opposing bound was found by repeatedly subtracting

the previous step size times the sign of the residual from λ_1^{n-1} until a point where a residual of opposite sign was found. Brent's method with tol $= 10^{-10}$ was ran for 100 iterations.[4]

3 Results

In our analysis, $4,216$ viscoelastic models were compared and tested across 144 testing conditions. Due to the amount of data, selected results are presented in the main body of the paper highlighting key outcomes and conclusions. Additional results are presented in the *Supplementary Materials*. Further, modeling results were organized hierarchically into an ordered list so that the extensive amount of data can be examined systematically. The classical and fractional forms are then further divided into three groups, Maxwell, Kelvin-Voigt and Zener, with the Zener forms further divided into 8 groups corresponding to $a_1 = 0.01$ to 0.8. The 8 Maxwell forms are listed from $a_1 = 0.01$ to 0.8, the 6 Kelvin-Voigt forms are listed from $b_1 = 0.2$ to 20, and the 6 forms from each Zener group are listed from $b_1 = 0.2$ to 20 throughout the rest of the analysis. This order of model form is maintained throughout the presentation of the results.

To organize the results, the similarity scores between the model forms were reordered in this fashion and compiled into mosaic plots. To find the comparison between two specific models, the position of each model on the legend can be found by 1) first picking out whether the modeling approach is classical or fractional, and if fractional what parameters α_a and α_b were used, then 2) the specific form of Maxwell, Kelvin-Voigt, or Zener, and finally 3) the parameters a_1 and b_1 of the model (Fig. 5A). Their positions on the legend points to a specific block within the mosaic plot which is shown by the red and blue arrows in Fig. 5B. The color of each block represents the similarity metric (Eq. (28)) computed from the gray lines representing the difference between the blue and red curves, which corresponds to the color of the models selected in Fig. 5A (Fig. 5C). In the following sections, we examine how the responses of these model forms change in different kinematics testing setups - with the maximum strain applied, the nonlinearity of the material behavior, and the frequency of loading.

3.1 Model Response Under Varying Kinematic Conditions

Figure 6 shows how the different model forms compare to each other under sinusoidal cyclic uniaxial stretch of $1/1.2$ to 1.2 and a nonlinearity parameter of $c_1 = 2$. Each cell of the array plot shows the similarity score (Eq. (28)) between two specific model forms. The diagonal indicate the comparison between the same forms (with a score of 0), and are thus colored black. The plot is symmetric by definition and thus the top triangle is used for the response at 5 Hz and the bottom triangle is used to show the response at 0.05 Hz (0.5 Hz were also tested but not shown). The results show significantly different behavior at each frequency.

Notably, the classical forms show significantly higher scores on average. At 0.05 Hz, the classical Maxwell forms in particular show significant differences with the other forms (Fig. 6). The classical Kelvin-Voigt and Zener forms compare well with the fractional forms, except when b_1 is small. This is due to the fact that small b_1 values reduce to a pure elastic

---

[4]If no solution was found, the *differential_evolution* method (from SciPy module [146]) was ran over the bounded range of $[0.6, (150/c_1)^{1/4}]$ (with the upperbound chosen to prevent double overflow), with tol $=$ 1e-12, popsize $= 21$ and other default settings.
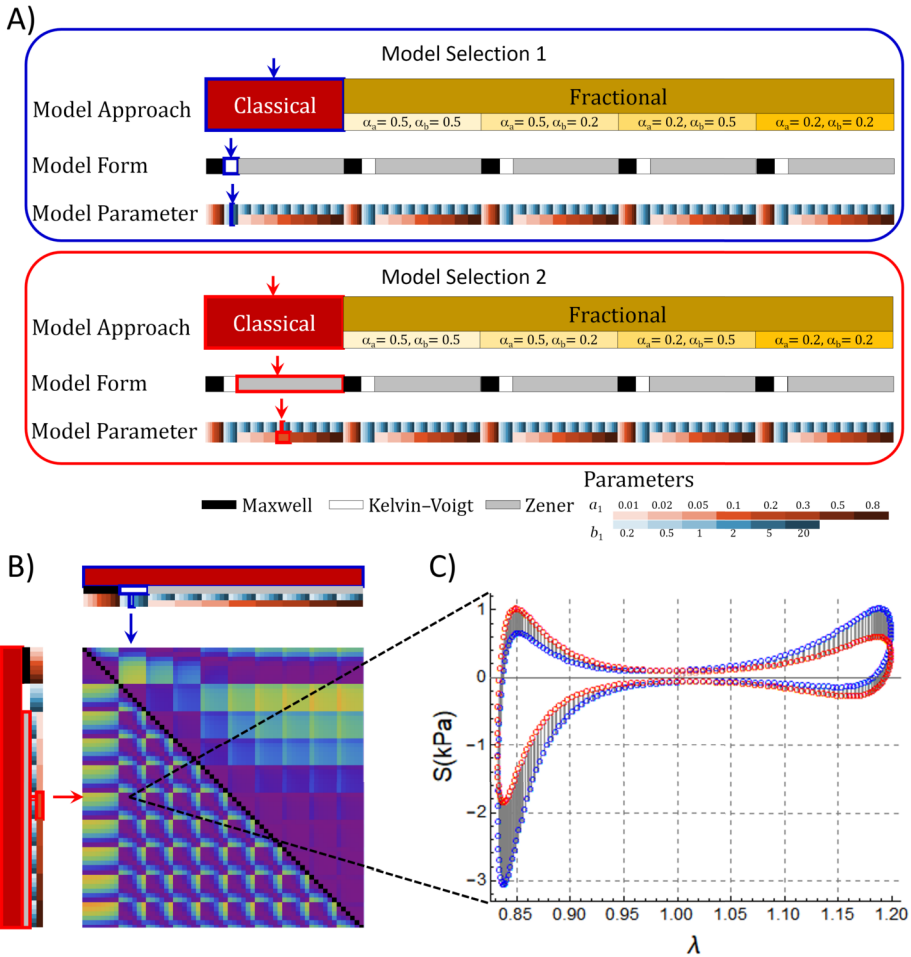
Fig. 5 Illustration of the mosaic plots and their interpretation. Simulations were ran for all combinations of models forms and model parameters listed in Sect. 2.4.3. The resulting model responses were compared in pairs (Eq. (28)) and compiled into mosaic plots in Fig. 6 and for other kinematics shown in the Appendix. **A)** Illustrates how to find the location for the comparison between two models by 1) looking up whether the modeling approach is classical or fractional and if fractional, then what parameters α_a and α_b were used, then 2) the specific form of Maxwell, Kelvin-Voigt, or Zener, and finally 3) the parameters a_1 and b_1 of the model. **B)** Once their position on the legend are found, they point to a specific block within the mosaic plot. **C)** The color of each block represents the similarity metric (Eq. (28)) computed from the gray lines representing the difference between the blue and red curves, which corresponds to the color of the models selected in **A)**

response on the right hand side. The fractional forms are generally very consistent, especially for its Zener forms. On the contrary, some of the trends seem to reverse at 5 Hz. The classical Maxwell form behaves much more comparably with the other forms, while the Kelvin-Voigt forms and Zener forms with small a_1 values are outliers (note Zener forms with low a_1 values reduce to the Kelvin-Voigt form). The fractional forms also seem to bias against high b_1 values more often. These types of behaviors illustrate how the b_1 terms become more dominate at high frequencies and how the a_1 term can heavily dampen the rate dependent change in response.
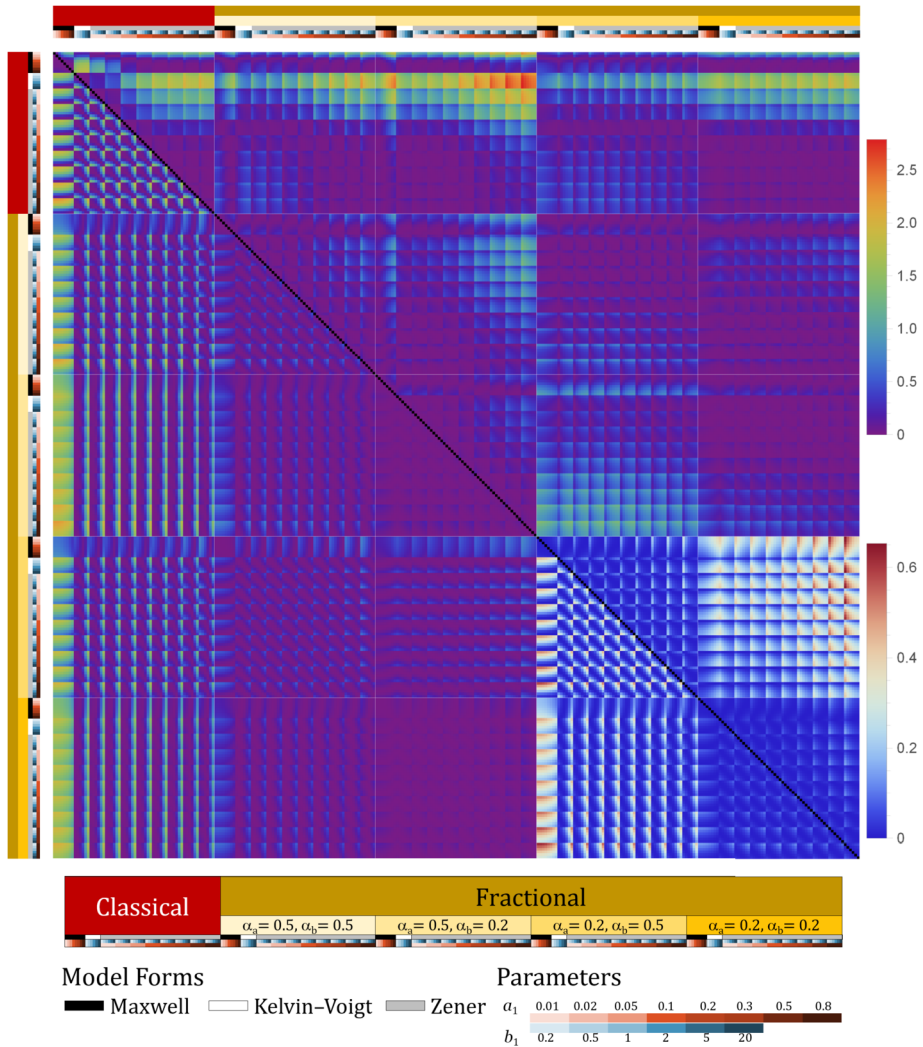
Fig. 6 An illustration using cyclic uniaxial extension with a sine wave form as the example to show how the model responses compare to each other. Each cell shows the similarity score (Eq. (28)) between two model forms. The bottom half of the array plot shows the comparison with a frequency of loading of 0.05 Hz and the top half at 5 Hz. The plots for $\alpha_a = 0.2$ uses a different color scale to show more details. Note the general consistency of the fractional forms and the low score of the classical Maxwell and Kelvin-Voigt forms at 0.05 Hz. However, this trend can reverse at higher frequencies, where classical Maxwell and Kelvin-Voigt forms achieve low scores and fractional models vary significantly more in their responses

To examine more closely, we compared each form against a representative specimen (Sect. 2.4.3), plotted their similarity score (Fig. 7 left) and the best case normalized stress strain curves for the classical Maxwell, Kelvin-Voigt and Zener forms (Fig. 7 right). For the classical and fractional Zener models, 8 values of a_1 are investigated. Together with the Maxwell and Kelvin-Voigt models, this leads to 10 color groups, each comprising 6 dots, for the 6 values of b_1 investigated. The right column shows the normalized response of the
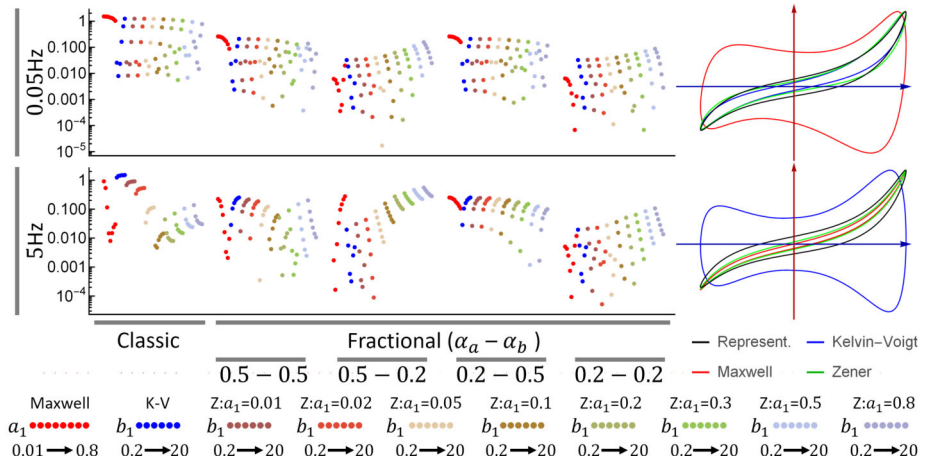
Fig. 7 Examination of each model form in comparison to a representative fractional Zener model exhibiting similar behavior to experimental data. Results at (top) 0.05 and (bottom) 5 Hz are shown. Scatter plots show the similarity scores (Eq. (28)) for each model form and parameter combination on the left and the behavior of the *best case* (lowest similarity score) classical Maxwell, Kelvin-Voigt and Zener models on the right. The dots of the same colors have different parameters increasing from left to right as indicated in the legend below the plots. The parameter a_1 is {0.01, 0.02, 0.05, 0.1, 0.2, 0.3, 0.5, 0.8} and the parameter b_1 are {0.2, 0.4, 1, 2, 5, 20}. Note the reverse in trend for the Maxwell and Kelvin-Voigt forms and the increase in selectivity for the fractional forms at higher frequency

best classical Maxwell, Kelvin-Voigt and Zener models, and a representative curve which was selected from the fractional Zener model iterations. As for Fig. 2, the red vertical axis is for the normalized stress, the blue horizontal axis is for normalized strain and the green alternative is for normalized time.

The most important difference in trend is the swap in behavior between varying the a_1 parameter and the b_1 parameter. At 0.05 Hz, each Kelvin-Voigt and Zener groups are arranged in a V-shaped pattern indicating an optimal response for a given b_1 value within each group. The Maxwell forms in this case tend to occur in a cluster with the trend of decreasing scores with a_1. On the contrary, at 5 Hz, the Maxwell forms are arranged in the V-shape while the Kelvin-Voigt and Zener forms are clustered. Interestingly, the Kelvin-Voigt and Zener groups form a V-shape showing the optimality for a specific a_1 value. We can observe this more clearly by examining the shape of the stress-strain curves (Fig. 7). The classical Maxwell model at 0.05 Hz leads to the most dissimilar curves across all tests, reflecting the high scores observed. The hysteresis is larger than for the other models. Additionally, there is a negative slope around the 0% stretch, as opposed to the other models which yield a positive slope. In contrast, the observed classical Kelvin-Voigt (blue) curves switch place with the Maxwell (red) at 5 Hz, yielding an abnormal response with high hysteresis.

We next repeated this analysis for the remaining kinematics, and the results for 0.05 Hz and $c_1 = 2$ are shown in Fig. 8. Broader frequency investigation of each kinematics, as presented in the uniaxial case in Fig. 6 and 7, is presented in the *Supplementary Materials*. In Fig. 8, the kinematics are arranged top to bottom as uniaxial (sinusoidal (A) and saw-like (B) deformations), biaxial (C), pure shear (D), simple shear (E), torsional shear (F), relaxation (G) and creep (H). Again, in the available data, the metric is only shown for the classical models and the fractional ones with $(\alpha_a, \alpha_b) \in \{(05, 0.5), (0.5, 0.2), (0.2, 0.5), (0.2, 0.2)\}$.
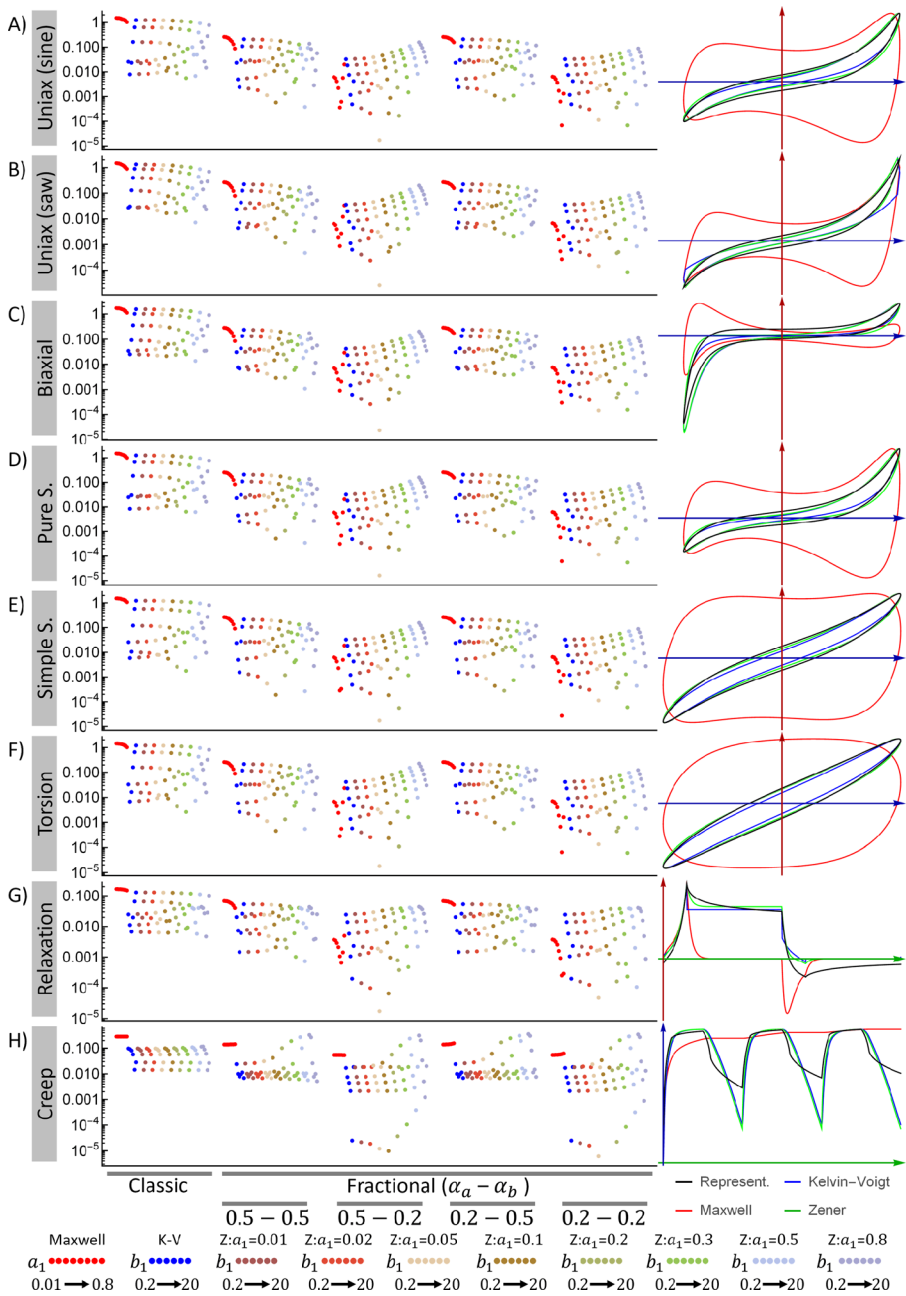
Fig. 8 Examination of each model form in comparison to a representative fractional Zener model exhibiting similar behavior to experimental data for varying kinematics test cases (at 0.05 Hz). Results are shown for **A)** uniaxial (sine), **B)** uniaxial (saw), **C)** biaxial (sine), **D)** pure shear (sine), **E)** simple shear (sine), **F)** torsion (sine), **G)** relaxation, and **H)** creep. Scatter plots show the similarity scores (Eq. (28)) for each model form and parameter combination on the left and the behavior of the *best case* (lowest similarity score) classical Maxwell, Kelvin-Voigt and Zener models on the right. The dots of the same colors have different parameters increasing from left to right as indicated in the legend below the plots. The parameter a_1 are $\{0.01, 0.02, 0.05, 0.1, 0.2, 0.3, 0.5, 0.8\}$ and the parameter b_1 are $\{0.2, 0.4, 1, 2, 5, 20\}$

The abnormal behavior of the classical Maxwell model can be observed here for all kinematics. In the relaxation test, although the decay part of the curve shows a power-law decrease, the plateauing part of the stress quickly reaches 0, which is atypical of tissues (Fig. 2). For the unloading path, due to the viscous stresses and absence of elastic ones, the Maxwell model produces the largest resistance when the strain is reduced from $\lambda = 1.2$ to 1, leading to a stress undershoot before decaying again to 0. The fractional adaption of the Maxwell model can be tweaked to produce better results except for the creep test, where the dissimilarity would remain high. Under several cycles of applying a constant load and then unloading, the Maxwell models would lead to a continuous increase in strain, with no recovery.

The classical Kelvin-Voigt and Zener models show similar results across the tests' range, particularly in the oscillatory tests. Note, however, that for the uniaxial test using a saw-type loading, a jump in the stress level is recorded for the classical Kelvin-Voigt model. This is because the abrupt change between loading and unloading, under the derivative, leads to a sudden positive to negative stress change, which is only partly corrected by the elastic term. The classical Zener model provides a better continuity in this sense. For the relaxation test, both models decay to the elastic stress level, but with the Kelvin-Voigt form decaying instantaneously at the end of the loading phase. As the strain decreases, the viscous part in both models leads to an undershoot, before the stress settles to 0. Note that this is smaller than for the Maxwell model due to the presence of the elastic term. For the creep and release test, both classical Kelvin-Voigt and Zener models see a gradual strain increase during the constant load phase, then a sudden, almost linear decrease during the recovery. Over multiple creep and release tests the recovery strain drifts higher. A fractional approach of both Kelvin-Voigt and Zener models improves the similarity with the representative curves across all tests. Although pictured only for the fractional Zener (chosen as representative), the relaxation curve decays gradually towards the elastic limit, as exhibited in tissues in literature (Fig. 2). The strain decrease leads to a stress undershoot, which slowly relaxes towards 0. The creep and release test shows a gradual strain increase, followed by a gradual, non-complete recovery, which drifts higher across multiple tests. The low dissimilarity score suggests that the same can be inferred about the fractional Kelvin-Voigt model. Note that the creep test's similarity scores show a clearer differentiation of parameters that are suitable for reproducing a representative behavior. Therefore, this test can help single out optimal parameters from a wider range of satisfactory combinations.

3.2 Optimal Model Form for Material Nonlinearity

Here, we examine the models' behavior for two exponential parameters ($c_1 = 1$ and $c_1 = 4$), for two stretch ratios ($\lambda = 1/1.1$ to 1.1 and $\lambda = 1/1.4$ to 1.4). In Fig. 9, the impact of the exponential parameter and deformation level are shown for the uniaxial test, with the other tests being presented in the *Supplementary Materials*. The organisation of Fig. 9 is similar to before, with the left column showing the similarity metric of the classical and fractional models (for some parameter combinations) compared to a representative case, and the right column showing the normalised best classical models curves compared to the same representative curve. For both stretch ratios, an increase in the exponential parameter c_1 leads to noticeable differences. For a stretch of $\lambda = 1.1$, the models' response deviates more from an elliptical path. However, for a larger stretch ($\lambda = 1.4$), not only does the general trend of the curves change, but the hysteresis also diminishes, relative to the peak stress level achieved. Among the models, it is once again evident that the classical Maxwell formulation for low frequencies leads to responses that are not representative of those observed in tissues,
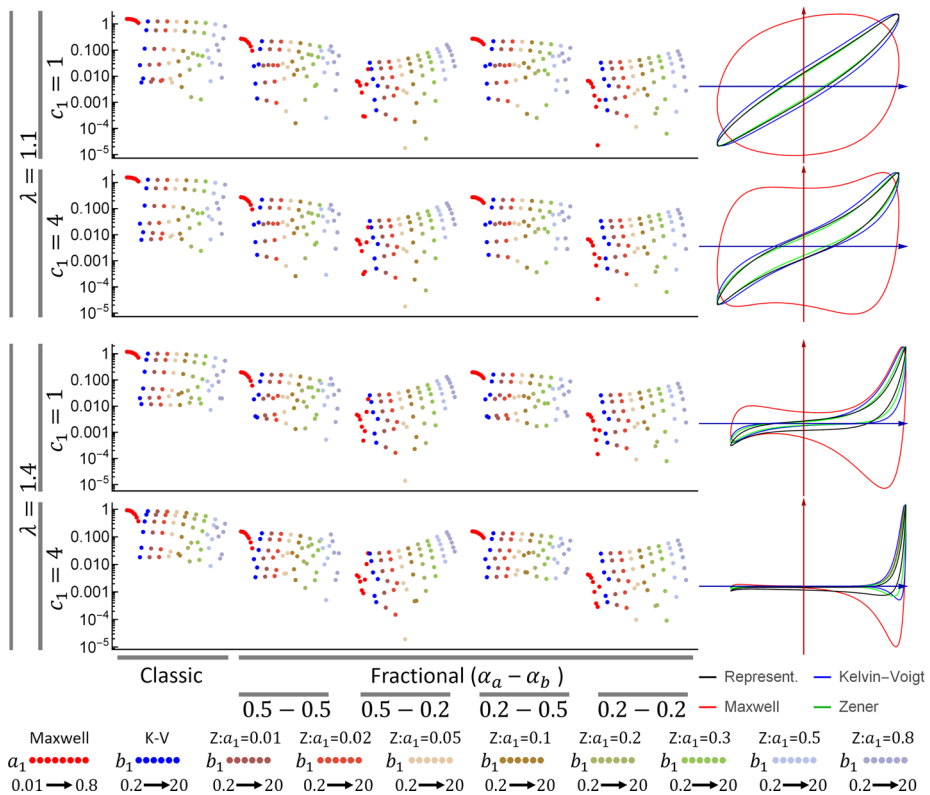
Fig. 9 Results shown the similarity scores at the maximum stretch of 1.1 and 1.4 (row 1&2 and 3&4, respectively) and two different nonlinearity parameters $c_1 = 1$ and $c_1 = 4$ (row 1&3 and 2&4, respectively). The dots of the same colors have different parameters increasing from left to right as indicated in the legend below the plots. The parameter a_1 are $\{0.01, 0.02, 0.05, 0.1, 0.2, 0.3, 0.5, 0.8\}$ and the parameter b_1 are $\{0.2, 0.4, 1, 2, 5, 20\}$. Interestingly, the comparison of model responses is not significantly affected by the material nonlinearity (c_1 parameter). However, a difference in the optimal parameter values (a_1 and b_1) are observed at larger loading strain. This seems to be due, in part, to the larger strains being more capable at changing the effective nonlinearity of the material response than simply the exponent c_1

yet a fractional approach would improve this aspect. The classical Kelvin-Voigt and Zener models appear to approach well the representative fractional Zener curve for a stretch of 1.1. However, at large stretches, the classical forms undershoot when switching from loading to unloading. A fractional approach would help in this sense, as indicated by the similarity metric. Overall, here we infer that by increasing the deformation level within a test can improve the identification of the exponent parameter.

3.3 Optimal Model Form for Frequency of Loading

To better investigate the effect of the frequency (rate) of loading, we examined the storage and loss moduli in the range $10^{-3} - 10^3$ Hz. The simulations were reduced to the uniaxial case with a maximum strain of 1% and a nonlinearity of $c_1 = 0.5$. Figures 10 and 11 show the storage and loss moduli (E' and E'', respectively) of the classical and fractional models, where the layout indicates the varying parameters. Note that, due to the models considered being incompressible isotropic, the trends describe the shear storage and loss moduli (G'
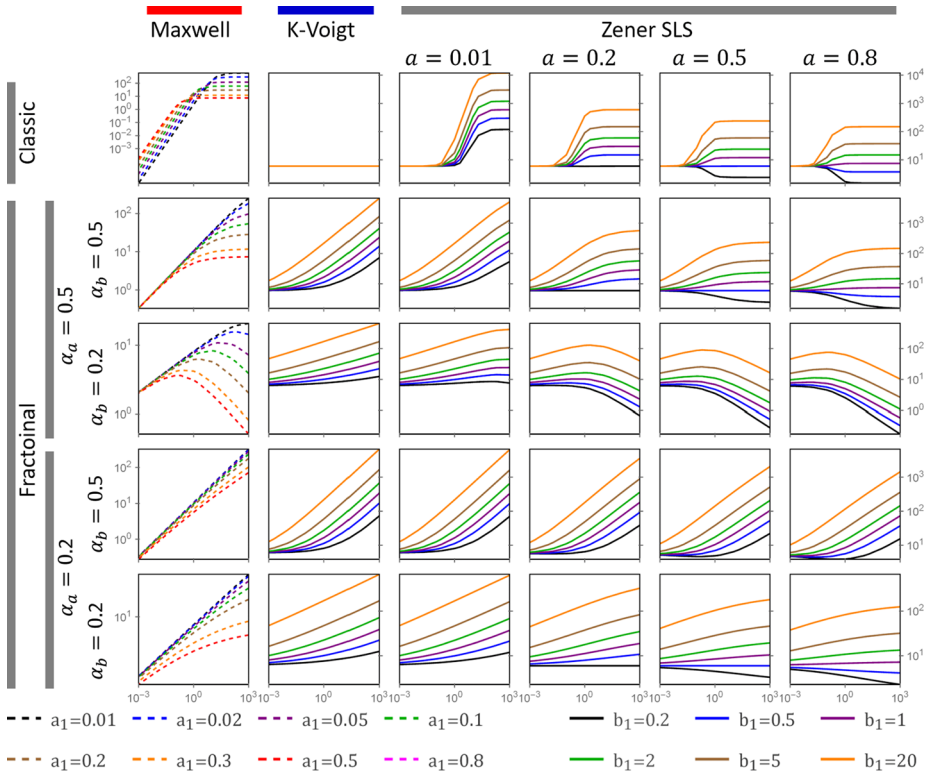
Fig. 10 The small strain storage moduli are shown for all considered model forms. Each subplot shows the storage moduli (kPa) vs the frequency (Hz). For the Maxwell forms, the scaling is shown on the left. For the remaining forms, the scaling is shown on the right. The Maxwell form curves correspond to different parameters a_1, rather than b_1 as for the other model forms, and are thus plotted with dashed line. From top to bottom, the models are arranged by (top row) classical and (row 2-5) fractional forms of different α_a and α_b values. The order is similar to Fig. 6. From left to right, Maxwell, Kelvin-Voigt and Zener model forms with different a_1 are considered (either classical or fractional). For each individual plot, multiple parameters are shown considering the other free model parameter. Note that Maxwell plots use dashed lines to indicate that a different parameter is being varied as well as the axis range on the left side, while all other plots use the axis range on the right

and G'') as well, as $E = 3G$. As a general overview, the first column shows the results for the Maxwell model, the second column for the Kelvin-Voigt, and columns 3-6 for the Zener model, while the top row corresponds to the classical model forms and rows 2-5 correspond to the fractional counterparts. For the Zener models, the linear parameter a_1, which scales the total stress derivative $D_t^{\alpha_a} \mathbf{S}_{ve}$, increases from the 3$^{\text{rd}}$ to the 6$^{\text{th}}$ column, taking the values 0.01, 0.2, 0.5 and 0.8. The fractional order parameter α_a varies across the row groups 2-3 and 4-5, ranging between 0.5 and 0.2, respectively. For each fixed α_a value, the α_b fractional order also ranges between 0.5 and 0.2 (hence the 2×2 groups of rows). For the classical and fractional Maxwell models, each figure shows 8 dashed curves corresponding to a_1 values of 0.01, 0.02, 0.05, 0.1, 0.2, 0.3, 0.5 and 0.8, while the b_1 parameter is 1. For the Kelvin-Voigt and Zener models, there are 6 solid lines which indicate that the b_1 parameter varies between 0.2, 0.5, 1, 2, 5 and 20. In the case of the Maxwell group, the storage and loss moduli axes are located on the left of each figure, while for the Kelvin-Voigt and Zener groups, the axes
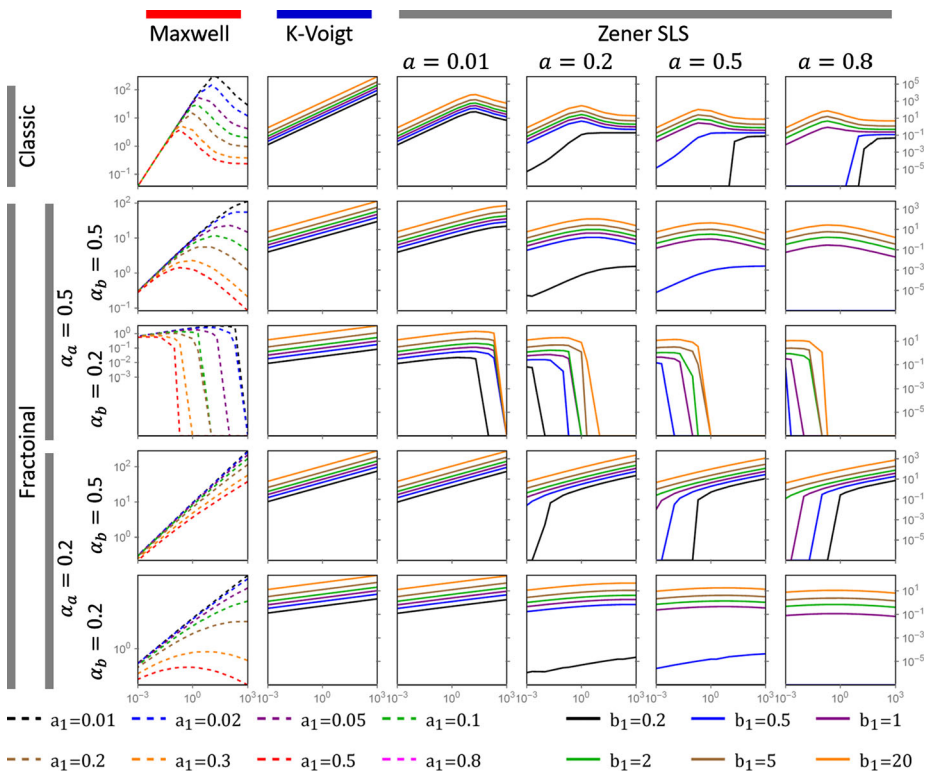
Fig. 11 The small strain loss moduli are shown for all various model forms. From top to bottom, the models are arranged by (top row) classical and (row 2-5) fractional forms of different α_a and α_b values. Each subplot shows the loss moduli (kPa) vs the frequency (Hz). For the Maxwell forms, the scaling is shown on the left. For the remaining forms, the scaling is shown on the right. The Maxwell form curves correspond to different parameters a_1, rather than b_1 as for the other model forms, and are thus plotted with dashed line. The order is similar to Fig. 6. From left to right, Maxwell, Kelvin-Voigt and Zener model forms with different a_1 are considered (either classical or fractional). For each individual plot, multiple parameters are shown considering the other free model parameter. Note that Maxwell plots use dashed lines to indicate that a different parameter is being varied as well as the axis range on the left side, while all other plots use the axis range on the right

are located on the right hand size of the 6th column. With this layout in mind, it can be observed that the fractional Kelvin-Voigt response is repetitive between row groups 2-3 and 4-5, as the varying parameter α_a does not appear in the formulation of these models and thus does not influence the response.

Typical frequency behavior varies across tissues and range of frequency employed, but some general trends can be identified. Often, both storage and loss moduli increase with frequency following a power law [35, 105], which may transition from a weaker to a stronger power law when the upper range of the frequency is increased [17, 26, 62]. Alternatively, both moduli may appear as increasing with frequency and then plateauing [86], and the loss modulus may even follow a descending trend after an initial increase [13, 88, 142]. Across the board, we can see that some models or parameter combinations do not yield any of the expected trends. A fractional order α_a larger than α_b leads to a decrease of the storage modulus towards the end tail of the frequency range, while the loss modulus vanishes after reaching a peak value. Even for cases when $\alpha_a \leq \alpha_b$, when the linear scaling parameter b_1

is smaller than a_1 in the Zener models, the storage modulus follows a decreasing trend or a decrease followed by an increase, while the loss modulus becomes negligible for most of the frequency spectrum. On the same note, an increasing a_1 parameter in the Maxwell models (where $\alpha_a = \alpha_b$ and $b_1 = 1$) leads to an increase and then decrease of the loss modulus even below the initial levels reached at low frequencies. Therefore, for models that employ derivatives on the viscoelastic stress as well as on the total stress, it is advisable that the order of the viscoelastic stress derivative is higher than that of the total stress. Bagley and Torvik [10] found that, for the fractional Zener model to be well-defined across any frequency range, α_a and α_b must be equal. It is also preferable that the scaling parameter of the viscoelastic stress be higher than the one of the total stress, especially if the fractional orders are equal. If these conditions are satisfied, then varying the a_1 parameter can help modulate the frequency at which the storage modulus plateaus or changes from a weak to a strong power law behavior, and the loss modulus plateaus or reverses from an increasing to a decreasing trend. The maximum storage and loss moduli achieved could be altered through the a_1 parameter, but parameter b_1 is more impactful in this sense. The Kelvin-Voigt models capture a power law behavior of the loss and storage moduli, which may be tailored to transition from a weaker to a stronger power law through the manipulation of the fractional order α_b and the linear scaling b_1 in the case of the storage modulus. However, it does not appear to capture a plateauing storage modulus behavior, or an increase followed by a decrease for the loss modulus.

4 Discussion

This study analyzes the behavior of the nonlinear classical Maxwell, Kelvin-Voigt and Zener models and their viscoelastic adaptions under typical kinematic conditions imposed in rheology testing. An extensive parameter examination was carried out, with models relying upon up to 6 parameters, each spanning several values. Section 3 presented the models' behavior under specific conditions or parameters, and here we aim to overview and gather the knowledge gained from those analyses. We will start from the fractional Zener model, as it provides the most generality, and then consider the simplifications that lead to the classical, Maxwell or Kelvin-Voigt forms (Fig. 4), and their impact on the tests studied.

The most comprehensive model considered in this study is fractional Zener (Eq. (17)) and entails 6 parameters. Its versatility allows it to capture typical tissue behavior in oscillatory, constant stress, constant load and frequency tests. The similarity metric for the fractional Zener model indicates an extensive choice of parameters that can be employed to replicate typical tissue behavior. However, this is also an indicator on the extensive rheological testing that needs to be performed in order to identify a unique set of optimal parameters. Indeed, under limited frequency regimes, the fractional Zener model can be seen to behave similarly to simpler models (depending on the test considered).

The classical Zener model effectively reduces the fractional model complexity by setting both derivative orders α_a and α_b to 1 (Eq. (13)), and thus relying upon 4 parameters. This simplification leads to significant changes in the relaxation and creep tests. During a constant applied strain, the model decays rapidly to a constant (elastic) stress level. The short relaxation time is atypical of tissues, as seen in Fig. 2. The creep shows a characteristic tissue response during the constant load phase but not during the release, where the strain decreases linearly. Therefore, the classical Zener model might be ill suited to model tissue behavior under high impact (*e.g.,* abdominal organs in a car crash), or the heart for growth and remodeling problems, where loading triggers the growth.

A further model simplification would be achieved by dismissing the elastic stress and setting $b_0 = 0$, leading to a classical Maxwell model. In all the curves shown at a small loading rate (0.05 Hz in Figs. 8 and 9), the model failed to capture a representative behavior, mostly due to excessive hysteresis. Therefore, it is unsuitable to be employed with slow rate behavior, *e.g.,* the liver response under respiratory motion. Nonetheless, at faster deformation rates, the hysteresis diminished (Fig. 7). The fractional approach of the Maxwell model also appears to be able to produce representative tissue behavior, as it arises from the similarity metric, and is not restricted by the deformation rate. However, the pitfall of both classical and fractional Maxwell models remains their inability to predict creep behavior, as the strain keeps increasing indefinitely and there is no strain recovery during the offload periods. Hence this class of models is to be avoided for scenarios involving persistent mechanical stresses.

Another avenue of simplifying the Zener model is by setting the a_1 parameter to 0, leading to the Kelvin-Voigt type of models. This is particularly attractive because the ordinary differential equation becomes easier to implement and solve. The classical form exhibits the expected limitations in modeling relaxation behavior, which appears to decay instantly. Moreover, at higher frequency rates in oscillatory tests, the hysteresis amplifies to non-physiological levels (Fig. 7). This also reflects in the frequency behavior over a wider range, as the storage modulus remains constant but the loss modulus has an increasing trend (Figs. 10 and 11). Therefore, the classical Kelvin-Voigt model should not be employed with fast rate phenomena (*e.g.,* elastography applications). The fractional model approach is better suited for relaxation and frequency investigation for both slow and fast rates, and appears to be an attractive alternative to the fractional Zener model, from numerical and parameter fitting process perspectives. Its limitation arises from the frequency spectrum investigation, which reveals a continuous increasing path for both the storage and loss moduli. The frequency range over which these moduli increase according to a power-law, before plateauing, varies across tissues - *e.g.,* 0.01-10 Hz for liver [88] and cardiac thin filaments [142], 0.1-100 Hz in kidney [105]. Therefore, the use of the fractional Kelvin-Voigt model may have limitations in some elastography applications, or for modeling cardiac tissue dynamics.

Rheological testing of tissues has grown over the decades. It is now acknowledged that tissues generally exhibit nonlinearity and viscoelasticity, among other more specific traits. When planning rheological testing, it is advantageous to have an insight into how different protocols might accentuate certain features and help towards a better identification of model parameters. In this study we saw that, for an isotropic material, uniaxial and shear deformation lead towards a similar behavior being exhibited (Fig. 8), hence choosing a single test out of the two could help avoiding redundancy. Biaxial stretching enables a better differentiation between the quasi-linear behavior and the transition to nonlinearity, hence being preferable for characterizing a model's nonlinearity - exponent c_1. An increase in the stretching level has a similar effect in accentuating model nonlinearity (Fig. 9), but a careful tissue handling is required in order to avoid damage. The inclusion of a purely elastic term in the model is essential for modeling creep behavior, as seen from the inadequate shape of the Maxwell type of models. However, the fractional Maxwell model appears to be able to capture a representative behavior across all other tests. This indicates a possible redundancy of the elastic term across the other kinematics, which could lead to non-unique parameter identification. For example, a previous study involving the fractional Kelvin-Voigt model [23] indicated that appropriate torque response could be achieved with either a combination of large b_0 and α_b values or small α_b and $b_0 = 0$. Although this could be a consequence of employing similar forms for $\mathbf{S}_e$ and $\mathbf{S}_Q$ in both this study and [23], the inclusion of a purely elastic term is essential and could be well characterized through a combination of tests. In

the above example, a relaxation test would have helped in identifying the b_0 and α_b balance, as a small relaxation time (large α_b) would have led to a rapid decay towards the elastic limit $b_0 \mathbf{S}_e$, whereas a small α_b would have shown a slow decay. Apart from the stress decay in relaxation tests, fractional parameters α_a and α_b also modulate the hysteresis levels, hence cyclic tests are required in determining their contribution. Generally it should be considered that $\alpha_a \leq \alpha_b$, as otherwise the loss modulus shows non-physiological trends (Fig. 11).

We note that Bagley and Torvik [10] show, for a linear fractional Zener model, that $\alpha_a = \alpha_b$ to satisfy the second law of thermodynamics under cyclic load. While non-dissipative behavior was not observed in the tests presented, for the case where $(\alpha_a, \alpha_b) = (0.2, 0.5)$, $a_1 = 0.8$, $b_0, b_1, c_0 = 1$ and frequencies below ≈ 0.0025 Hz, hysteresis amounted in a small accumulation of energy as opposed to a dissipation. Although this only occurs for small frequencies, this indeed suggest that $\alpha_a = \alpha_b$ or $\alpha_a = 0$ is necessary to satisfiy the laws of thermodynamic.

The storage and loss moduli investigation over an extensive frequency range can also point towards the appropriate balanced contribution of a_1 and b_1, as a_1 can modulate the frequency at which these moduli stop increasing according to a power-law, and b_1 can tailor the maximum level achieved. From this analysis it can be inferred that for a more complex model, like fractional Zener, an extensive testing is required in order to be able to separate parameter contribution - an oscillatory test at large stretch levels, creep, relaxation and frequency range investigation. If the latter is not available, then the use of the fractional Kelvin-Voigt model might be preferable, to avoid $\alpha_a - \alpha_b$ ambiguity.

4.1 Limitations

In this study some assumptions and simplifications had to be adopted, due to the extensive amount of data produced by parameter variation. Firstly, the models were limited to be isotropic. Anisotropic forms would have shown a more pronounced differences between uniaxial and shear responses, whereas a redundancy of the two modes of deformation was observed here. Nonetheless, based on the knowledge gained in this study, a model with predefined set of feasible parameters (*e.g.*, $\alpha_a \leq \alpha_b$ and $a_1 \leq b_1$) can be extended to incorporate anisotropic forms for which the material parameters can be determined from further studies. Secondly, here the same underlying form was assumed for $\mathbf{S}_e$ and $\mathbf{S}_Q$, with $c_1^e = c_1^v$. These forms could be altered, but the gain would not have been significant for the purpose of this study, whose focus is on the viscoelastic behavior exhibited by different model forms, rather than on the underlying hyperelastic behavior. Moreover, other types of material models could have been employed in lieu of the Fung-type model. For example, a study considering fractional viscoelastic models with Mooney-Rivlin, Fung and Ogden forms for a limited number of rheological tests is done in [23]. Nevertheless, considering multiple forms here would have further complicated the analysis of results, which currently consists of 4,216 models compared across 144 testing conditions. Model complexity could also be increased, *e.g.*, by incorporating additional viscoelastic terms ($b_2 D_t^{\alpha_c} \mathbf{S}_Q$). However, as the fractional Zener model showed enough versatility to capture typical tissue behavior across several testing protocols, additional terms might have simply led to redundancy in observed behavior. However, this idea might be pursued in combination with increasing material complexity, such as anisotropy.

The visual results presented in this study had to be narrowed down to several representative cases. More parameter combinations results are available in the *Supplementary Materials*, but an exhaustive representation would have been impossible due to the large number of curves produced. Nonetheless we believe that the discussion points addressed in Sects. 3 and 4 offer a good overview on models' capabilities and parameter influence.

5 Conclusions

Viscoelastic modeling of biological tissues is an area that has been explored to some extent in literature, but lags behind hyperelastic modeling amongst modelers. Classical viscoelastic models have been more readily employed, while fractional formulations have only been emerging more recently. The study presented here offers a systematic overview of nonlinear classical Maxwell, Kelvin-Voigt, Zener and their fractional model adaptions across a range of typical rheological tests. Different kinematic tests have been imposed (oscillatory uniaxial and shear deformations, constant load and constant strain), as well as variations in deformation level and frequency response. A comprehensive model parameter analysis was also performed across a broad spectrum, revealing the specific influence of each parameter on model behavior. While the results could not be presented exhaustively, due to the large number of curves produced, the relevant information was inferred by computing a similarity metric of each model-parameter combination against all the other combinations, or against a representative curve. Therefore, we could identify the scenarios which yield typical tissue responses, as well as understand the limitations of the other cases. As such, the findings of this study can be used in making an informed model selection when aiming to capture particular rheological traits. Alternatively, the insights gained here can help devising testing protocols such that model parameters can be well identified from varying tissue response.

Choosing an appropriate viscoelastic model depends on the behavior that needs to be replicated. If a simple, uniaxial cyclic stress response has to be characterized, then the classical Zener model would suffice. At low frequencies, a further simplification to classical Kelvin-Voigt model would work (*i.e.,* $a_1 = 0$), whereas for intermediate to high frequencies, the simplification should be done towards the Maxwell form (*i.e.,* $b_0 = 0$). Similarly, if relaxation and creep responses are not of interest, then one can select a simpler model like Maxwell or Kelvin-Voigt in order to replicate other types of behavior (*e.g.,* cyclic). However, for realistic responses across a wide range of tests and frequencies, the fractional Zener model is the most robust, if employed with a reasonable set of parameters. This model could always be considered as a general starting point, with simplifications being carried as appropriate, depending on frequency range of interest and deformation type - cyclic or constant stress/strain.

6 Acknowledgements

Author Contribution Will Zhang and Adela Capilnasiu acknowledge equal contributions toward first authorship.

References

1. Adolfsson, K., Enelund, M.: Fractional derivative viscoelasticity at large deformations. Nonlinear Dyn. **33**(3), 301–321 (2003)
2. Aggarwal, A., Aguilar, V.S., Lee, C.H., Ferrari, G., Gorman, J.H., Gorman, R.C., Sacks, M.S.: Patient-specific modeling of heart valves: from image to simulation. In: Ourselin, S., Rueckert, D., Smith, N. (eds.) Functional Imaging and Modeling of the Heart, pp. 141–149. Springer, Berlin (2013)
3. Alexander, H., Cook, T.: Accounting for natural tension in the mechanical testing of human skin. J. Invest. Dermatol. **69**(3), 310–314 (1977)
4. Anssari-Benam, A., Bader, D.L., Screen, H.R.C.: A combined experimental and modelling approach to aortic valve viscoelasticity in tensile deformation. J. Mater. Sci., Mater. Med. **22**(2), 253–262 (2011)
5. Antoniadis, A.P., Mortier, P., Kassab, G., Dubini, G., Foin, N., Murasato, Y., Giannopoulos, A.A., Tu, S., Iwasaki, K., Hikichi, Y., Migliavacca, F., Chiastra, C., Wentzel, J.J., Gijsen, F., Reiber, J.H., Barlis, P., Serruys, P.W., Bhatt, D.L., Stankovic, G., Edelman, E.R., Giannoglou, G.D., Louvard, Y., Chatzizi-sis, Y.S.: Biomechanical modeling to improve coronary artery bifurcation stenting. JACC: Cardiovasc. Interv. **8**(10), 1281–1296 (2015)
6. Asner, L., Hadjicharalambous, M., Chabiniok, R., Peresutti, D., Sammut, E., Wong, J., Carr-White, G., Chowienczyk, P., Lee, J., King, A., Smith, N., Razavi, R., Nordsletten, D.: Estimation of passive and active properties in the human heart using 3d tagged MRI. Biomech. Model. Mechanobiol. **15**(5), 1121–1139 (2015)
7. Asner, L., Hadjicharalambous, M., Chabiniok, R., Peressutti, D., Sammut, E., Wong, J., Carr-White, G., Razavi, R., King, A., Smith, N., Nordsletten, D.: Patient-specific modeling for left ventricular mechanics using data-driven boundary energies. Comput. Methods Appl. Mech. Eng. **314**, 269–295 (2017)
8. Avazmohammadi, R., Soares, J.S., Li, D.S., Raut, S.S., Gorman, R.C., Sacks, M.S.: A contemporary look at biomechanical models of myocardium. Annu. Rev. Biomed. Eng. **21**(1), 417–442 (2019)
9. Ayyildiz, M., Cinoglu, S., Basdogan, C.: Effect of normal compression on the shear modulus of soft tissue in rheological measurements. J. Mech. Behav. Biomed. Mater. **49**, 235–243 (2015)
10. Bagley, R.L., Torvik, P.J.: On the fractional calculus model of viscoelastic behavior. J. Rheol. **30**(1), 133–155 (1986)
11. Balbi, V., Shearer, T., Parnell, W.J.: A modified formulation of quasi-linear viscoelasticity for transversely isotropic materials under finite deformation. Proc. R. Soc. A, Math. Phys. Eng. Sci. **474**(2217), 20180, 231 (2018)
12. Bao, Y., Wu, D., Yan, Z., Du, Z.: A new hybrid viscoelastic soft tissue model based on meshless method for haptic surgical simulation. Open Biomed. Eng. J. **7**(1), 116–124 (2013)
13. Bilston, L.E., Liu, Z., Phan-Thien, N.: Large strain behaviour of brain tissue in shear: some experimental data and differential constitutive model. Biorheology **38**, 335–345 (2001)
14. Bischoff, J.E., Arruda, E.M., Grosh, K.: Finite element modeling of human skin using an isotropic, nonlinear elastic constitutive model. J. Biomech. **33**(6), 645–652 (2000)
15. Bonet, J., Wood, R.: Nonlinear Continuum Mechanics for Finite Element Analysis. Cambridge University Press, Cambridge (1997)
16. Bonet, J., Wood, R.D.: Nonlinear Continuum Mechanics for Finite Element Analysis, 2nd edn. Cambridge University Press, Cambridge (2008)
17. Bonfanti, A., Kaplan, J.L., Charras, G., Kabla, A.: Fractional viscoelastic models for power-law materials. Soft Matter **16**(26), 6002–6020 (2020)
18. Bonifasi-Lista, C., Cherkaev, E., Yeni, Y.N.: Analytical approach to recovering bone porosity from effective complex shear modulus. J. Biomech. Eng. **131**(12), 121003 (2009)
19. Brent, R.P.: An algorithm with guaranteed convergence for finding a zero of a function. Comput. J. **14**(4), 422–425 (1971)
20. Budday, S., Sommer, G., Holzapfel, G., Steinmann, P., Kuhl, E.: Viscoelastic parameter identification of human brain tissue. J. Mech. Behav. Biomed. Mater. **74**, 463–476 (2017)
21. Budday, S., Ovaert, T.C., Holzapfel, G.A., Steinmann, P., Kuhl, E.: Fifty shades of brain: a review on the mechanical testing and modeling of brain tissue. Arch. Comput. Methods Eng. **27**(4), 1187–1230 (2019)
22. Canovic, E.P., Qing, B., Mijailovic, A.S., Jagielska, A., Whitfield, M.J., Kelly, E., Turner, D., Sahin, M., Vliet, K.J.V.: Characterizing multiscale mechanical properties of brain tissue using atomic force microscopy, impact indentation, and rheometry. J. Vis. Exp. **2016**(115), 54201 (2016)

23. Capilnasiu, A., Bilston, L., Sinkus, R., Nordsletten, D.: Nonlinear viscoelastic constitutive model for bovine liver tissue. Biomech. Model. Mechanobiol. **19**(5), 1641–1662 (2020)

24. Cavinato, C., Helfenstein-Didier, C., Olivier, T., du Roscoat, S.R., Laroche, N., Badel, P.: Biaxial loading of arterial tissues with 3d in situ observations of adventitia fibrous microstructure: a method coupling multi-photon confocal microscopy and bulge inflation test. J. Mech. Behav. Biomed. Mater. **74**, 488–498 (2017)

25. Chabiniok, R., Moireau, P., Lesault, P.F., Rahmouni, A., Deux, J.F., Chapelle, D.: Estimation of tissue contractility from cardiac cine-MRI using a biomechanical heart model. Biomech. Model. Mechanobiol. **11**(5), 609–630 (2011)

26. Chatelin, S., Oudry, J., Périchon, N., Sandrin, L., Allemann, P., Soler, L., Willinger, R.: In vivo liver tissue mechanical properties by transient elastography: comparison with dynamic mechanical analysis. Biorheology **48**(2), 75–88 (2011)

27. Christensen, R.M.: A nonlinear theory of viscoelasticity for application to elastomers. J. Appl. Mech. **47**(4), 762–768 (1980)

28. Chui, C., Kobayashi, E., Chen, X., Hisada, T., Sakuma, I.: Combined compression and elongation experiments and non-linear modelling of liver tissue for surgical simulation. Med. Biol. Eng. Comput. **42**(6), 787–798 (2004)

29. Clin, J., Aubin, C.E., Parent, S., Sangole, A., Labelle, H.: Comparison of the biomechanical 3d efficiency of different brace designs for the treatment of scoliosis using a finite element model. Eur. Spine J. **19**(7), 1169–1178 (2010)

30. Coleman, B.D., Noll, W.: Erratum: foundations of linear viscoelasticity. Rev. Mod. Phys. **36**(4), 1103 (1964)

31. Corr, D.T., Starr, M.J., Vanderby, R., Best, T.M.: A nonlinear generalized Maxwell fluid model for viscoelastic materials. J. Appl. Mech. **68**(5), 787–790 (2001)

32. Cua, A.B., Wilhelm, K.P., Maibach, H.I.: Elastic properties of human skin: relation to age, sex, and anatomical region. Arch. Dermatol. Res. **282**(5), 283–288 (1990)

33. Demer, L.L., Yin, F.C.: Passive biaxial mechanical properties of isolated canine myocardium. J. Physiol. **339**(1), 615–630 (1983)

34. Demiray, H.: A note on the elasticity of soft biological tissues. J. Biomech. **5**(3), 309–311 (1972)

35. Deng, L., Trepat, X., Butler, J.P., Millet, E., Morgan, K.G., Weitz, D.A., Fredberg, J.J.: Fast and slow dynamics of the cytoskeleton. Nat. Mater. **5**(8), 636–640 (2006)

36. Doehring, T.C., Freed, A.D., Carew, E.O., Vesely, I.: Fractional order viscoelasticity of the aortic valve cusp: an alternative to quasilinear viscoelasticity. J. Biomech. Eng. **127**(4), 700–708 (2005)

37. Dokos, S., Smaill, B.H., Young, A.A., LeGrice, I.J.: Shear properties of passive ventricular myocardium. Am. J. Physiol., Heart Circ. Physiol. **283**(6), H2650–H2659 (2002)

38. Flügge, W.: Viscoelasticity. Springer, Berlin (1975)

39. Forte, A.E., Gentleman, S.M., Dini, D.: On the characterization of the heterogeneous mechanical response of human brain tissue. Biomech. Model. Mechanobiol. **16**(3), 907–920 (2016)

40. Fortier, A., Gullapalli, V., Mirshams, R.A.: Review of biomechanical studies of arteries and their effect on stent performance. IJC Heart Vessels **4**, 12–18 (2014)

41. Freed, A.D., Diethelm, K.: Fractional calculus in biomechanics: a 3d viscoelastic model using regularized fractional derivative kernels with application to the human calcaneal fat pad. Biomech. Model. Mechanobiol. **5**(4), 203–215 (2006)

42. Fulcher, G.R., Hukins, D.W., Shepherd, D.E.: Viscoelastic properties of bovine articular cartilage attached to subchondral bone at high frequencies. BMC Musculoskelet. Disord. **10**(1), 61 (2009)

43. Fung, Y.: Elasticity of soft tissues in simple elongation. Am. J. Physiol.-Legacy Content **213**(6), 1532–1544 (1967)

44. Fung, Y.C.: Biomechanics. Springer, New York (1993)

45. Fung, Y.C., Fronek, K., Patitucci, P.: Pseudoelasticity of arteries and the choice of its mathematical expression. Am. J. Physiol., Heart Circ. Physiol. **237**(5), H620–H631 (1979)

46. Funk, J.R., Hall, G.W., Crandall, J.R., Pilkey, W.D.: Linear and quasi-linear viscoelastic characterization of ankle ligaments. J. Biomech. Eng. **122**(1), 15–22 (1999)

47. Gao, Z., Lister, K., Desai, J.P.: Constitutive modeling of liver tissue: experiment and theory. Ann. Biomed. Eng. **38**(2), 505–516 (2009)

48. Gao, H., Li, W.G., Cai, L., Berry, C., Luo, X.Y.: Parameter estimation in a Holzapfel–Ogden law for healthy myocardium. J. Eng. Math. **95**(1), 231–248 (2015)

49. García, A., Martínez, M., Peña, E.: Viscoelastic properties of the passive mechanical behavior of the porcine carotid artery: influence of proximal and distal positions. Biorheology **49**(4), 271–288 (2012)

50. Gasser, T.C., Miller, C.: Patient-Specific Simulation of Abdominal Aortic Aneurysms pp. 1–14. Springer, Berlin (2018)

51. Gasser, T.C., Ogden, R.W., Holzapfel, G.A.: Hyperelastic modelling of arterial layers with distributed collagen fibre orientations. J. R. Soc. Interface **3**(6), 15–35 (2005)

52. Geerligs, M.M.: Skin layer mechanics. Ph.D. thesis, Technische Universiteit Eindhoven (2010)

53. Ghajari, M., Hellyer, P.J., Sharp, D.J.: Computational modelling of traumatic brain injury predicts the location of chronic traumatic encephalopathy pathology. Brain **140**(2), 333–343 (2017)

54. Gijsen, F.J., Migliavacca, F., Schievano, S., Socci, L., Petrini, L., Thury, A., Wentzel, J.J., van der Steen, A.F., Serruys, P.W., Dubini, G.: Simulation of stent deployment in a realistic human coronary artery. Biomed. Eng. Online **7**(1), 23 (2008)

55. Gonzalez-Blohm, S.A., Doulgeris, J.J., Lee, W.E., Shea, T.M., Aghayev, K., Vrionis, F.D.: The current testing protocols for biomechanical evaluation of lumbar spinal implants in laboratory setting: a review of the literature. BioMed Res. Int. **2015**, 1–15 (2015)

56. Green, M.S., Tobolsky, A.V.: A new approach to the theory of relaxing polymeric media. J. Chem. Phys. **14**(2), 80–92 (1946)

57. Groves, R.B., Coulman, S.A., Birchall, J.C., Evans, S.L.: An anisotropic, hyperelastic model for skin: experimental measurements, finite element modelling and identification of parameters for human and murine skin. J. Mech. Behav. Biomed. Mater. **18**, 167–180 (2013)

58. Gültekin, O., Sommer, G., Holzapfel, G.A.: An orthotropic viscoelastic model for the passive myocardium: continuum basis and numerical treatment. Comput. Methods Biomech. Biomed. Eng. **19**(15), 1647–1664 (2016)

59. Hadjicharalambous, M., Asner, L., Chabiniok, R., Sammut, E., Wong, J., Peressutti, D., Kerfoot, E., King, A., Lee, J., Razavi, R., Smith, N., Carr-White, G., Nordsletten, D.: Non-invasive model-based assessment of passive left-ventricular myocardial stiffness in healthy subjects and in patients with non-ischemic dilated cardiomyopathy. Ann. Biomed. Eng. **45**(3), 605–618 (2016)

60. Hildebrandt, J., Fukaya, H., Martin, C.: Simple uniaxial and uniform biaxial deformation of nearly isotropic incompressible tissues. Biophys. J. **9**(6), 781–791 (1969)

61. Hilfer, R.: Fractional diffusion based on Riemann-Liouville fractional derivatives. J. Phys. Chem. B **104**(16), 3914–3917 (2000)

62. Holt, B., Tripathi, A., Morgan, J.: Viscoelastic response of human skin to low magnitude physiologically relevant shear. J. Biomech. **41**(12), 2689–2695 (2008)

63. Holzapfel, G.A.: Nonlinear Solid Mechanics: A Continuum Approach for Engineering. John Wiley & Sons, Hoboken (2000)

64. Holzapfel, G.A., Ogden, R.W.: Constitutive modelling of passive myocardium: a structurally based framework for material characterization. Philos. Trans. R. Soc. A, Math. Phys. Eng. Sci. **367**(1902), 3445–3475 (2009)

65. Holzapfel, G.A., Simo, J.C.: A new viscoelastic constitutive model for continuous media at finite thermomechanical changes. Int. J. Solids Struct. **33**, 3019–3034 (1996)

66. Holzapfel, G.A., Gasser, T.C., Ogden, R.W.: A new constitutive framework for arterial wall mechanics and a comparative study of material models. J. Elast. **61**(1/3), 1–48 (2000)

67. Horgan, C.O.: The remarkable gent constitutive model for hyperelastic materials. Int. J. Non-Linear Mech. **68**, 9–16 (2015)

68. Horgan, C.O., Saccomandi, G.: A description of arterial wall mechanics using limiting chain extensibility constitutive models. Biomech. Model. Mechanobiol. **1**(4), 251–266 (2003)

69. Hurschler, C., Loitz-Ramage, B., Vanderby, R.: A structurally based stress-stretch relationship for tendon and ligament. J. Biomech. Eng. **119**(4), 392–399 (1997)

70. Jansen, L.E., Birch, N.P., Schiffman, J.D., Crosby, A.J., Peyton, S.R.: Mechanics of intact bone marrow. J. Mech. Behav. Biomed. Mater. **50**, 299–307 (2015)

71. Johnson, G.A., Tramaglini, D.M., Levine, R.E., Ohno, K., Choi, N.Y., Woo, S.L.Y.: Tensile and viscoelastic properties of human patellar tendon. J. Orthop. Res. **12**(6), 796–803 (1994)

72. Jones, D.F., Treloar, L.R.G.: The properties of rubber in pure homogeneous strain. J. Phys. D, Appl. Phys. **8**(11), 1285–1304 (1975)

73. Jordan, P., Socrate, S., Zickler, T., Howe, R.: Constitutive modeling of porcine liver in indentation using 3d ultrasound imaging. J. Mech. Behav. Biomed. Mater. **2**(2), 192–201 (2009)

74. Jordan, P., Kerdok, A.E., Howe, R.D., Socrate, S.: Identifying a minimal rheological configuration: a tool for effective and efficient constitutive modeling of soft tissues. J. Biomech. Eng. **133**(4), 041006 (2011)

75. Karami, G., Grundman, N., Abolfathi, N., Naik, A., Ziejewski, M.: A micromechanical hyperelastic modeling of brain white matter under large deformation. J. Mech. Behav. Biomed. Mater. **2**(3), 243–254 (2009)

76. Karimi, A., Haghighatnama, M., Shojaei, A., Navidbakhsh, M., Haghi, A.M., Sadati, S.J.A.: Measurement of the viscoelastic mechanical properties of the skin tissue under uniaxial loading. Proc. Inst. Mech. Eng., Part L, J. Mater., Des. Appl. **230**(2), 418–425 (2015)

77. Kashan, J.S., Ali, S.M.: Modeling and simulation for mechanical behavior of modified biocomposite for scaffold application. Ing. Investig. **39**(1), 63–75 (2019)

78. Kaye, A., Stepto, R.F.T., Work, W.J., Alemán, J.V., Malkin, A.Y.: Definition of terms relating to the non-ultimate mechanical properties of polymers (recommendations 1998). Pure Appl. Chem. **70**(3), 701–754 (1998)

79. Kearney, S.P., Khan, A., Dai, Z., Royston, T.J.: Dynamic viscoelastic models of human skin using optical elastography. Phys. Med. Biol. **60**(17), 6975–6990 (2015)

80. Kerdok, A.E., Ottensmeyer, M.P., Howe, R.D.: Effects of perfusion on the viscoelastic characteristics of liver. J. Biomech. **39**(12), 2221–2231 (2006)

81. Khosravi, A., Bani, M.S., Bahreinizad, H., Karimi, A.: Viscoelastic properties of the autologous bypass grafts: a comparative study among the small saphenous vein and internal thoracic artery. Artery Res. **19**(C), 65 (2017)

82. Klatt, D., Hamhaber, U., Asbach, P., Braun, J., Sack, I.: Noninvasive assessment of the rheological behavior of human organs using multifrequency MR elastography: a study of brain and liver viscoelasticity. Phys. Med. Biol. **52**(24), 7281–7294 (2007)

83. Krishnamurthy, A., Villongco, C.T., Chuang, J., Frank, L.R., Nigam, V., Belezzuoli, E., Stark, P., Krummen, D.E., Narayan, S., Omens, J.H., McCulloch, A.D., Kerckhoffs, R.C.: Patient-specific models of cardiac biomechanics. J. Comput. Phys. **244**, 4–21 (2013)

84. Lakes, R.S.: Viscoelastic Solids (1998), 1st edn. CRC Press, Boca Raton (2017)

85. Lau, K., Diaz, V., Scambler, P., Burriesci, G.: Mitral valve dynamics in structural and fluid–structure interaction models. Med. Eng. Phys. **32**(9), 1057–1064 (2010)

86. Lawless, B.M., Sadeghi, H., Temple, D.K., Dhaliwal, H., Espino, D.M., Hukins, D.W.: Viscoelasticity of articular cartilage: analysing the effect of induced stress and the restraint of bone in a dynamic environment. J. Mech. Behav. Biomed. Mater. **75**, 293–301 (2017)

87. Levin, A., Wyman, J., Hill, A.V.: The viscous elastic properties of muscle. Proc. R. Soc. Lond., B Contain. Pap. Biol. Character **101**(709), 218–243 (1927)

88. Liu, Z., Bilston, L.: On the viscoelastic character of liver tissue: experiments and modelling of the linear behaviour. Biorheology **37**, 191–201 (2000)

89. Machado, J.T., Kiryakova, V., Mainardi, F.: Recent history of fractional calculus. Commun. Nonlinear Sci. Numer. Simul. **16**(3), 1140–1153 (2011)

90. Magin, R.L.: Fractional calculus in bioengineering. Crit. Rev. Biomed. Eng. **32**, 1–104 (2004)

91. Mainardi, F.: Fractional Calculus and Waves in Linear Viscoelasticity: An Introduction to Mathematical Models. Imperial College Press, London (2010)

92. Mano, J.F.: Viscoelastic properties of bone: mechanical spectroscopy studies on a chicken model. Mater. Sci. Eng. C **25**(2), 145–152 (2005)

93. Marescaux, J., Clément, J.M., Tassetti, V., Koehl, C., Cotin, S., Russier, Y., Mutter, D., Delingette, H., Ayache, N.: Virtual reality applied to hepatic surgery simulation: the next revolution. Ann. Surg. **228**(5), 627–634 (1998)

94. Mariappan, Y.K., Glaser, K.J., Ehman, R.L.: Magnetic resonance elastography: a review. Clin. Anat. **23**(5), 497–511 (2010)

95. Martins, P.A.L.S., Jorge, R.M.N., Ferreira, A.J.M.: A comparative study of several material models for prediction of hyperelastic properties: application to silicone-rubber and soft tissues. Strain **42**(3), 135–147 (2006)

96. May-Newman, K., Lam, C., Yin, F.C.P.: A hyperelastic constitutive law for aortic valve tissue. J. Biomech. Eng. **131**(8), 081009 (2009)

97. Mazzia, A., Pini, G.: Product Gauss quadrature rules vs. cubature rules in the meshless local Petrov–Galerkin method. J. Complex. **26**(1), 82–101 (2010)

98. Meaney, D.F.: Relationship between structural modeling and hyperelastic material behavior: application to CNS white matter. Biomech. Model. Mechanobiol. **1**(4), 279–293 (2003)

99. Mendis, K.K., Stalnaker, R.L., Advani, S.H.: A constitutive relationship for large deformation finite element modeling of brain tissue. J. Biomech. Eng. **117**(3), 279–285 (1995)

100. Meyers, M.A., Chawla, K.K.: Mechanical Behavior of Materials. Cambridge University Press, Cambridge (2008)

101. Mihai, L.A., Goriely, A.: How to characterize a nonlinear elastic material? A review on nonlinear constitutive parameters in isotropic finite elasticity. Proc. R. Soc. A, Math. Phys. Eng. Sci. **473**(2207), 20170607 (2017)

102. Mihai, L.A., Budday, S., Holzapfel, G.A., Kuhl, E., Goriely, A.: A family of hyperelastic models for human brain tissue. J. Mech. Phys. Solids **106**, 60–79 (2017)

103. Miller, K., Chinzei, K.: Constitutive modelling of brain tissue: experiment and theory. J. Biomech. **30**(11–12), 1115–1121 (1997)

104. Moreira, D., Nunes, L.: Comparison of simple and pure shear for an incompressible isotropic hypere-lastic material under large deformation. Polym. Test. **32**(2), 240–248 (2013)

105. Nasseri, S., Bilston, L.E., Phan-Thien, N.: Viscoelastic properties of pig kidney in shear, experimental results and modelling. Rheol. Acta **41**(1–2), 180–192 (2002)

106. Nishimura, S., Nagai, S., Katoh, M., Yamashita, H., Saeki, Y., ichi Okada, J., Hisada, T., Nagai, R., Sugiura, S.: Microtubules modulate the stiffness of cardiomyocytes against shear stress. Circ. Res. **98**(1), 81–87 (2006)

107. O'Toole, R.V., Jaramaz, B., DiGioia, A.M., Visnic, C.D., Reid, R.H.: Biomechanics for preoperative planning and surgical simulations in orthopaedics. Comput. Biol. Med. **25**(2), 183–191 (1995)

108. Ogden, R.W.: Non-linear Elastic Deformations. Dover, New York (1997)

109. Ogden, R.W., Hill, R.: Large deformation isotropic elasticity - on the correlation of theory and exper-iment for incompressible rubberlike solids. Proc. R. Soc. Lond. Ser. A, Math. Phys. Sci. **326**(1567), 565–584 (1972)

110. Oliphant, T.E.: A Guide to NumPy, vol. 1. Trelgol Publishing, USA (2006)

111. Parker, K.J., Szabo, T., Holm, S.: Towards a consensus on rheological models for elastography in soft tissues. Phys. Med. Biol. **64**(21), 215012 (2019)

112. Peirlinck, M., Costabal, F.S., Sack, K.L., Choy, J.S., Kassab, G.S., Guccione, J.M., Beule, M.D., Segers, P., Kuhl, E.: Using machine learning to characterize heart failure across the scales. Biomech. Model. Mechanobiol. **18**(6), 1987–2001 (2019)

113. Pfensig, S., Arbeiter, D., Kohse, S., Grabow, N., Schmitz, K.P., Kaule, S., Stiehm, M., Siewert, S.: De-velopment of a constitutive law for numerical simulation of artificial leaflet-structures for transcatheter heart valve prostheses. Curr. Dir. Biomed. Eng. **5**(1), 569–572 (2019)

114. Picton, D., Wills, D.: Viscoelastic properties of the periodontal ligament and mucous membrane. J. Prosthet. Dent. **40**(3), 263–272 (1978)

115. Pinto, J.G., Fung, Y.: Mechanical properties of the heart muscle in the passive state. J. Biomech. **6**(6), 597–616 (1973)

116. Pinto, J.G., Patitucci, P.J.: Creep in cardiac muscle. Am. J. Physiol., Heart Circ. Physiol. **232**(6), H553–H563 (1977)

117. Podlubny, I.: Fractional Differential Equations: An Introduction to Fractional Derivatives, Fractional Differential Equations, to Methods of Their Solution and Some of Their Applications, vol. 198. Aca-demic Press, San Diego (1998)

118. Polio, S.R., Kundu, A.N., Dougan, C.E., Birch, N.P., Aurian-Blajeni, D.E., Schiffman, J.D., Crosby, A.J., Peyton, S.R.: Cross-platform mechanical characterization of lung tissue. PLoS ONE **13**(10), e0204765 (2018)

119. Polzer, S., Gasser, T.C., Bursa, J., Staffa, R., Vlachovsky, R., Man, V., Skacel, P.: Importance of material model in wall stress prediction in abdominal aortic aneurysms. Med. Eng. Phys. **35**(9), 1282–1289 (2013)

120. Qian, L., Todo, M., Morita, Y., Matsushita, Y., Koyano, K.: Deformation analysis of the periodontium considering the viscoelasticity of the periodontal ligament. Dent. Mater. **25**(10), 1285–1292 (2009)

121. Ramadan, S.T.: Development of an anthropomorphic dynamic heart phantom. Ph.D. thesis, University of Toronto (2017)

122. Reiter, R., Freise, C., Jöhrens, K., Kamphues, C., Seehofer, D., Stockmann, M., Somasundaram, R., Asbach, P., Braun, J., Samani, A., Sack, I.: Wideband MRE and static mechanical indentation of hu-man liver specimen: sensitivity of viscoelastic constants to the alteration of tissue structure in hepatic fibrosis. J. Biomech. **47**(7), 1665–1674 (2014)

123. Roan, E., Vemaganti, K.: The nonlinear material properties of liver tissue determined from no-slip uniaxial compression experiments. J. Biomech. Eng. **129**(3), 450–456 (2006)

124. Rosen, S.L.: Fundamental Principles of Polymeric Materials., John Wiley & Sons, Hoboken (1982)

125. Ross, B.: The development of fractional calculus 1695–1900. Hist. Math. **4**(1), 75–89 (1977)

126. Sacks, M.S., Drach, A., Lee, C.H., Khalighi, A.H., Rego, B.V., Zhang, W., Ayoub, S., Yoganathan, A.P., Gorman, R.C., Gorman, J.H.: On the simulation of mitral valve function in health, disease, and treatment. J. Biomech. Eng. **141**(7), 070804 (2019)

127. Schiessel, H., Blumen, A.: Hierarchical analogues to fractional relaxation equations. J. Phys. A, Math. Gen. **26**(19), 5057–5069 (1993)

128. Schiessel, H., Metzler, R., Blumen, A., Nonnenmacher, T.F.: Generalized viscoelastic models: their fractional equations with solutions. J. Phys. A, Math. Gen. **28**(23), 6567–6584 (1995)

129. Schmitt, C., Henni, A.H., Cloutier, G.: Ultrasound dynamic micro-elastography applied to the vis-coelastic characterization of soft tissues and arterial walls. Ultrasound Med. Biol. **36**(9), 1492–1503 (2010)

130. Sedov, L.I., Hodge, P.G.: Introduction to the mechanics of a continuous medium. J. Appl. Mech. **33**(1), 238 (1966)

131. Shearer, T.: A new strain energy function for the hyperelastic modelling of ligaments and tendons based on fascicle microstructure. J. Biomech. **48**(2), 290–297 (2015)
132. Sherifova, S., Holzapfel, G.A.: Biomechanics of aortic wall failure with a focus on dissection and aneurysm: a review. Acta Biomater. **99**, 1–17 (2019)
133. Sinkus, R., Siegmann, K., Xydeas, T., Tanter, M., Claussen, C., Fink, M.: MR elastography of breast lesions: understanding the solid/liquid duality can improve the specificity of contrast-enhanced MR mammography. Magn. Reson. Med. **58**(6), 1135–1144 (2007)
134. Sinkus, R., Lambert, S., Abd-Elmoniem, K.Z., Morse, C., Heller, T., Guenthner, C., Ghanem, A.M., Holm, S., Gharib, A.M.: Rheological determinants for simultaneous staging of hepatic fibrosis and inflammation in patients with chronic liver disease. NMR Biomed. **31**(10), e3956 (2018)
135. Soetens, J., van Vijven, M., Bader, D., Peters, G., Oomens, C.: A model of human skin under large amplitude oscillatory shear. J. Mech. Behav. Biomed. Mater. **86**(2018), 423–432 (2018)
136. Sommer, G., Schriefl, A.J., Andrä, M., Sacherer, M., Viertler, C., Wolinski, H., Holzapfel, G.A.: Biomechanical properties and microstructure of human ventricular myocardium. Acta Biomater. **24**, 172–192 (2015)
137. Sverre Grimnes, O.G.M.: Bioimpedance and Bioelectricity Basics. Academic Press, San Diego (2014)
138. Taber, L.A.: Nonlinear Theory of Elasticity. World Scientific, Singapore (2004)
139. Takamizawa, K., Hayashi, K.: Strain energy density function and uniform strain hypothesis for arterial mechanics. J. Biomech. **20**(1), 7–17 (1987)
140. Tan, K., Cheng, S., Jugé, L., Bilston, L.E.: Characterising soft tissues under large amplitude oscillatory shear and combined loading. J. Biomech. **46**(6), 1060–1066 (2013)
141. Tan, K., Cheng, S., Jugé, L., Bilston, L.E.: Characterising skeletal muscle under large strain using eccentric and Fourier transform-rheology. J. Biomech. **48**(14), 3788–3795 (2015)
142. Tassieri, M., Evans, R., Barbu-Tudoran, L., Trinick, J., Waigh, T.: The self-assembly, elasticity, and dynamics of cardiac thin filaments. Biophys. J. **94**(6), 2170–2178 (2008)
143. Taylor, D.C., Dalton, J.D., Seaber, A.V., Garrett, W.E.: Viscoelastic properties of muscle-tendon units. Am. J. Sports Med. **18**(3), 300–309 (1990)
144. Van Der Walt, S., Colbert, S.C., Varoquaux, G.: The NumPy array: a structure for efficient numerical computation. Comput. Sci. Eng. **13**(2), 22 (2011)
145. Veronda, D., Westmann, R.: Mechanical characterization of skin—finite deformations. J. Biomech. **3**(1), 111–124 (1970)
146. Virtanen, P., Gommers, R., Oliphant, T.E., Haberland, M., Reddy, T., Cournapeau, D., Burovski, E., Peterson, P., Weckesser, W., Bright, J., van der Walt, S.J., Brett, M., Wilson, J., Millman, K.J., Mayorov, N., Nelson, A.R.J., Jones, E., Kern, R., Larson, E., Carey, C.J., Polat, İ., Feng, Y., Moore, E.W., VanderPlas, J., Laxalde, D., Perktold, J., Cimrman, R., Henriksen, I., Quintero, E.A., Harris, C.R., Archibald, A.M., Ribeiro, A.H., Pedregosa, F., van Mulbregt, P., SciPy 1.0 Contributors: SciPy 1.0: fundamental algorithms for scientific computing in Python. Nat. Methods **17**, 261–272 (2020)
147. Vito, R.: A note on arterial elasticity. J. Biomech. **6**(5), 561–564 (1973)
148. Wang, S., Larin, K.V.: Optical coherence elastography for tissue characterization: a review. J. Biophotonics **8**(4), 279–302 (2014)
149. Wang, R., Sarntinoranont, M.: Biphasic analysis of rat brain slices under creep indentation shows nonlinear tension-compression behavior. J. Mech. Behav. Biomed. Mater. **89**, 1–8 (2019)
150. Wang, B.C., Wang, G.R., Yan, D.H., Liu, Y.P.: An experimental study on biomechanical properties of hepatic tissue using a new measuring method. Bio-Med. Mater. Eng. **2**(3), 133–138 (1992)
151. Wang, H.M., Luo, X.Y., Gao, H., Ogden, R.W., Griffith, B.E., Berry, C., Wang, T.J.: A modified holzapfel-ogden law for a residually stressed finite strain model of the human left ventricle in diastole. Biomech. Model. Mechanobiol. **13**(1), 99–113 (2013)
152. Wang, X., Schoen, J.A., Rentschler, M.E.: A quantitative comparison of soft tissue compressive viscoelastic model accuracy. J. Mech. Behav. Biomed. Mater. **20**, 126–136 (2013)
153. Weiss, J.A., Maker, B.N., Govindjee, S.: Finite element implementation of incompressible, transversely isotropic hyperelasticity. Comput. Methods Appl. Mech. Eng. **135**(1–2), 107–128 (1996)
154. Wex, C., Arndt, S., Stoll, A., Bruns, C., Kupriyanova, Y.: Isotropic incompressible hyperelastic models for modelling the mechanical behaviour of biological tissues: a review. Biomed. Eng./Biomed. Tech. **60**(6), 577–592 (2015)
155. Wiechert, E.: Gesetze der elastischen nachwirkung für constante temperatur. Ann. Phys. **286**(11), 546–570 (1893)
156. Wittek, A., Miller, K., Kikinis, R., Warfield, S.K.: Patient-specific model of brain deformation: application to medical image registration. J. Biomech. **40**(4), 919–929 (2007)
157. Wolfram Research, Inc.: Mathematica, Version 12.1. URL https://www.wolfram.com/mathematica, Champaign (2020)

158. Zadpoor, A.A., Malda, J.: Additive manufacturing of biomaterials, tissues, and organs. Ann. Biomed. Eng. **45**(1), 1–11 (2016)
159. Zener, C.: Elasticity and Anelasticity of Metals, 1st edn. University of Chicago Press, Chicago (1948)
160. Zhang, W., Capilnasiu, A., Sommer, G., Holzapfel, G.A., Nordsletten, D.A.: An efficient and accurate method for modeling nonlinear fractional viscoelastic biomaterials. Comput. Methods Appl. Mech. Eng. **362**, 112834 (2020)